

Structure and mechanogating of the mammalian tactile channel PIEZO2

Li Wang^{1,4}, Heng Zhou^{2,4}, Mingmin Zhang^{1,3,4}, Wenhao Liu^{1,3,4}, Tuan Deng¹, Qiancheng Zhao¹, Yiran Li¹, Jianlin Lei², Xueming Li^{2*} & Bailong Xiao^{1,3*}

PIEZO2 is a mechanosensitive cation channel that has a key role in sensing touch, tactile pain, breathing and blood pressure. Here we describe the cryo-electron microscopy structure of mouse **PIEZO2**, which is a three-bladed, propeller-like trimer that comprises 114 transmembrane helices (38 per protomer). Transmembrane helices 1–36 (TM1–36) are folded into nine tandem units of four transmembrane helices each to form the unusual non-planar blades. The three blades are collectively curved into a nano-dome of 28-nm diameter and 10-nm depth, with an extracellular cap-like structure embedded in the centre and a 9-nm-long intracellular beam connecting to the central pore. TM38 and the C-terminal domain are surrounded by the anchor domain and TM37, and enclose the central pore with both transmembrane and cytoplasmic constriction sites. Structural comparison between **PIEZO2** and its homologue **PIEZO1** reveals that the transmembrane constriction site might act as a transmembrane gate that is controlled by the cap domain. Together, our studies provide insights into the structure and mechanogating mechanism of Piezo channels.

PIEZO2, a member of the evolutionarily conserved mechanosensitive Piezo channel family, mediates mechanically activated and rapidly inactivating cationic currents in primary sensory neurons^{1,2}. Studies in mice that lack **PIEZO2** and in patients with loss-of-function mutations in **PIEZO2** have demonstrated its essential role in sensing gentle touch^{3–6}, tactile pain^{7,8}, proprioception^{5,9,10}, airway stretch and lung inflation¹¹, as well as in baroreceptors for sensing blood pressure and regulating heart rate¹². Furthermore, gain-of-function mutations in human **PIEZO2** have been associated with distal arthrogryposis^{5,13,14}, a genetic disorder that is characterized by severe joint contractures and restrictive lung diseases. Thus, **PIEZO2** represents a validated drug target for developing therapeutic agents such as analgesics for treating tactile pain.

Mammalian **PIEZO2** proteins are large membrane proteins that contain over 2,800 residues. **PIEZO2** proteins share only around 42% sequence homology with their homologue **PIEZO1**¹, which has about 2,500 residues and forms a three-bladed, propeller-like homotrimeric structure comprising a central ion-conducting pore module and three peripheral blades with 24 resolved transmembrane helices that are folded into six repeated transmembrane helical units (THUs). These six THUs, each composed of four transmembrane helices, are also termed the ‘Piezo repeats’^{15–19}. Here we have determined the homotrimeric structure of the full-length 2,822-residue mouse **PIEZO2** to a resolution of 3.6–3.8 Å, revealing a completely resolved topology of 38 transmembrane helices and a fully closed pore with both transmembrane and cytosolic constriction sites.

Determination of the structure of **PIEZO2**

The structure of mouse **PIEZO2** was determined by adopting a similar strategy to that used for **PIEZO1**¹⁶, but with substantial modifications (Extended Data Fig. 1, Methods, Supplementary Fig. 1). The optimized **PIEZO2** sample solubilized in the detergent glycol-diosgenin (GDN), which is a synthetic substitute for digitonin, allowed us to first obtain an overall 3.8 Å-resolution cryo-electron microscopy (cryo-EM) structure

(Extended Data Figs. 2, 3), which resembles the three-bladed, propeller-shaped structure of **PIEZO1**. With the exception of the extracellular cap (which was largely unresolved), all of the other structural domains that were observed in **PIEZO1** were resolved to 3.0–3.5 Å resolution in the **PIEZO2** structure (Extended Data Fig. 2e). A focused refinement of the central region led to a map of 3.86 Å resolution, which showed a much improved density for the cap domain (Extended Data Fig. 2c, f). In both **PIEZO1** and **PIEZO2** structures, the distal blade (which is encoded by the N-terminal 500–600 residues) was not resolved^{16,18,19}. We therefore performed focused refinements of the blade and distal blade domains and obtained maps of 3.64 Å and 3.77 Å resolution, respectively, which showed an additional 12 resolved transmembrane helices (Extended Data Fig. 2c, g, h).

The three focused maps (Extended Data Fig. 2f–h) were fitted together to generate the final map (Fig. 1, Extended Data Table 1), from which we were able to build a model by assigning 1,817 residues into the 38 transmembrane helices and the indicated domains that are shown in Fig. 2, Extended Data Figs. 4, 5 and Supplementary Fig. 2. The unassigned loop regions are listed in Supplementary Table 1. Collectively, we have for the first time—to our knowledge—resolved a complete 38-transmembrane-helix topology of **PIEZO2**.

The nano-dome configuration of the curved blades

The typical three-bladed, propeller-like structure of **PIEZO2** has an axial height of 170 Å and a diameter of 280 Å (Fig. 1a). The proximal transmembrane helices 25–38 (TM25–TM38) and the central region are supported by an intracellular beam that is 90 Å in length, and the peripheral TM1–TM24 hang at the distal end of the beam (Fig. 1a, c). The lack of apparent intracellular supporting structures for TM1–TM24 might explain the greater degree of flexibility of these helices relative to TM25–TM36. TM1–TM38 in each blade form a hydrophobic belt, and follow the ‘positive-inside’ rule for amino acid residues in membrane proteins²⁰ (Fig. 1b). Notably, the hydrophobic belt formed by the distal transmembrane helices of one subunit is located far above

¹State Key Laboratory of Membrane Biology, Beijing Advanced Innovation Center for Structural Biology, Tsinghua-Peking Joint Center for Life Sciences, IDG/McGovern Institute for Brain Research, School of Pharmaceutical Sciences, Tsinghua University, Beijing, China. ²MOE Key Laboratory of Protein Sciences, Beijing Advanced Innovation Center for Structural Biology, Tsinghua-Peking Joint Center for Life Sciences, School of Life Sciences, Tsinghua University, Beijing, China. ³Joint Graduate Program of Peking-Tsinghua-NIBS, School of Life Sciences, Tsinghua University, Beijing, China.

*These authors contributed equally: Li Wang, Heng Zhou, Mingmin Zhang, Wenhao Liu. *e-mail: lixueming@tsinghua.edu.cn; xbailong@mail.tsinghua.edu.cn

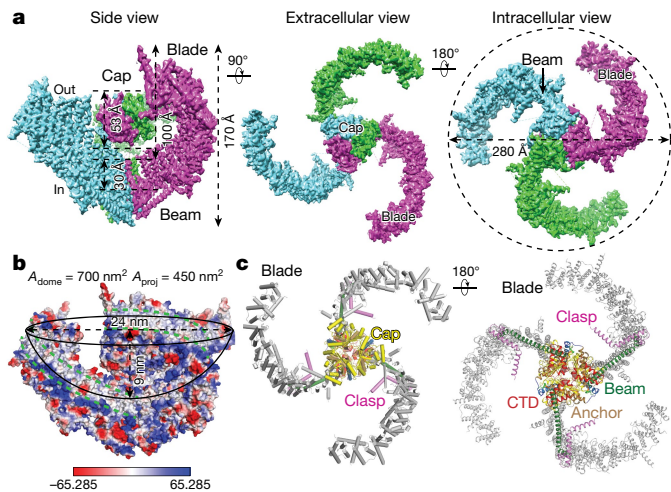


Fig. 1 | The homotrimeric structure of PIEZO2. **a**, The indicated views of the sharpened map (2.78σ contour level) with a resolution of 3.6–3.8 Å. **b**, A side view of the surface electrostatic potential, showing the hydrophobic transmembrane region (marked by green dashed lines). The mid-plane opening diameter, depth, surface area (A_{dome}) and projection area (A_{proj}) of the illustrated dome are labelled. The colour bar indicates the surface electrostatic potential, ranging from negative (red) to positive (blue). **c**, Cartoon models with the major structural domains coloured and labelled.

the belt formed by the proximal transmembrane helices of the neighbouring subunit (Fig. 1b). Accordingly, the transmembrane regions of the three blades are curved into a dome shape with a mid-plane opening diameter of approximately 24 nm and a depth of around 9 nm (outlined by the approximated sphere in Fig. 1b), which results in the extracellular cap domain being fully embedded in the centre (Fig. 1a, b). Given that reconstituted PIEZO1 proteins were able to curve the liposome membrane¹⁸, we expect that PIEZO2 might similarly deform the residing membrane, which might produce a mid-plane dome surface area of 700 nm² and a projected in-plane area of 450 nm² (Fig. 1b).

The 38-transmembrane-helix topological organization
Whereas TM37 and TM38 constitute the outer helix and inner helix, respectively, of the central pore module, TM1–TM36 are organized into nine repetitive THUs to form the highly curved blade (Fig. 2, Extended Data Fig. 5a–c). The resolved extracellular loops of the THUs lean against each other and form a flattened monolayer on the extracellular surface of the transmembrane blade (Extended Data Fig. 5a). Consistent with the proposed idea that parallel amphipathic helices represent a structural motif that is characteristic of inherently mechanosensitive channels²¹, each of THU2–THU9 is preceded by a helix that is parallel to the membrane, and these helices collectively form an intracellular helical layer directly below the membrane (Fig. 2a, Extended Data Fig. 5a–c). Such an organization of the extracellular loop layer and the intracellular helical layer might not only help to stabilize the non-planar transmembrane region of the blade and the residing membrane, but also facilitate mechanosensing and transduction.

The loop of around 540 residues that connects TM28 to TM29 (THU7 to THU8) represents the largest intracellular loop in PIEZO2 and contains the beam, latch and clasp domains (Fig. 2a, b). The distal part of the kinked beam is buried within a space enclosed by the intracellular side of THU7 and the clasp, and forms several pairs of hydrogen bonds with the clasp (Fig. 2b, Extended Data Fig. 5d). The proximal end of the beam directly connects to the latch domain and forms layered interfaces with the C-terminal domain (CTD), the anchor, the outer helix and the inner helix (Fig. 2b–e). These domains intertwine through polar interactions and hydrogen bonds (Extended Data Fig. 5e–g), which might allow them to function in concert to relay

the lever-like motion of the beam from the blade to the central pore (Extended Data Fig. 8b, e).

The ion-conducting pore

The C-terminal outer helix–cap–inner helix–CTD region trimerizes to form the central pore module (Fig. 2c, Extended Data Fig. 6a). Despite the existence of an extracellular vestibule inside the cap and potential opening of the top, the apparent fenestrations located in between the cap and the membrane region might allow cations to directly enter into the downstream transmembrane pore²² (Extended Data Fig. 6a, b). Consistent with this, the central cavity of the cap of PIEZO1 is reportedly not involved in ion permeation²³. We have therefore focused on analysing the transmembrane pore and the intracellular vestibule (Fig. 3). The inner helix, which is highly conserved between PIEZO2 and PIEZO1 (Fig. 3a), encloses the hydrophobic transmembrane pore (Fig. 3b, Extended Data Fig. 6k). In contrast to PIEZO1—which shows a wide and long side cavity between two inner helices—the membrane-facing side of the transmembrane region of PIEZO2 is fully sealed (Extended Data Fig. 6k). Notably, the membrane vestibule is flanked at the top by a constriction site of less than 1 Å radius that is formed by the residue L2743, and at the bottom by a 10 Å-long narrow pore region that is formed by the pore-facing residues V2750, F2754 and E2757 (Fig. 3a–c, Extended Data Fig. 4)—demonstrating a closed transmembrane pore. The two constriction sites of PIEZO2 at L2743, F2754 and E2757 are apparently dilated in the corresponding positions in PIEZO1 at L2469, F2480 and G2483, respectively (Fig. 3a–c, Extended Data Fig. 7d). We thus define the two transmembrane constriction sites as upper and lower transmembrane gates. E2757, which is the only negatively charged residue in the inner helix, faces the central pore axis (Fig. 3b) and controls the ion-permeating properties of PIEZO2. When this residue was mutated to alanine, the E2757A mutant exhibited a reduction of around 50% in the permeability of Ca²⁺ relative to Cs⁺ ($P_{\text{Ca}}/P_{\text{Cs}}$), when compared with wild-type PIEZO2 (wild-type versus E2757A: 1.34 ± 0.01 versus 0.63 ± 0.04) (Extended Data Fig. 6c–e), and a decrease of about 30% in single-channel conductance (wild-type versus E2757A: 24.1 ± 1.0 pS versus 16.7 ± 0.5 pS) (Extended Data Fig. 6g–j).

The transmembrane pore continues into the cytosol as an intracellular vestibule, and is followed by a 10 Å-long constriction neck that is formed by the residues M2767, P2810 and E2811 (Fig. 3b, c). A similar constriction neck formed by the corresponding residues M2493, P2536 and E2537 has previously been observed in PIEZO1^{16,18,19} (Fig. 3b, c, Extended Data Fig. 7d). In contrast to the E2757A mutant, neither PIEZO2(E2811A) nor PIEZO1(E2537A) showed changes in $P_{\text{Ca}}/P_{\text{Cs}}$ (Extended Data Fig. 6f). Furthermore, mutating M2493 in PIEZO1 did not affect the ion-permeation properties of the mutant protein¹⁹. Thus, this constriction neck does not appear to have a major role in controlling ion permeation.

In addition to the continuous central pore along the vertical axis, the intracellular vestibule has three apparent fenestrations sites (Extended Data Fig. 6k), which are open to three lateral portals (Extended Data Fig. 6l, m). Similar intracellular fenestrations and lateral portals exist in PIEZO1¹⁶ (Extended Data Fig. 6k). Residues E2769 and E2770 of PIEZO2 (or the corresponding E2495 and E2496 of PIEZO1) form a surface with a negative electrostatic potential in the lateral portal that connects to the intracellular vestibule (Fig. 3a, b, Extended Data Fig. 6k–m). Mutating these residues affects the ion-permeation properties of PIEZO1 and PIEZO2²², suggesting that the lateral portal might form an ion-conducting pathway.

Displacement of the transmembrane gate and the cap

Given the structural and functional resemblance between PIEZO1 and PIEZO2, we reasoned that conformational differences between PIEZO1 and PIEZO2 might provide insight into their mechanogating mechanism. Therefore, we aligned the PIEZO1 structures that were previously determined in the detergents digitonin (Protein Data Bank (PDB) accession: 6B3R)¹⁸, GDN (PDB: 6BPZ)¹⁹ or C₁₂E₁₀ (PDB: 5Z10)¹⁶ with

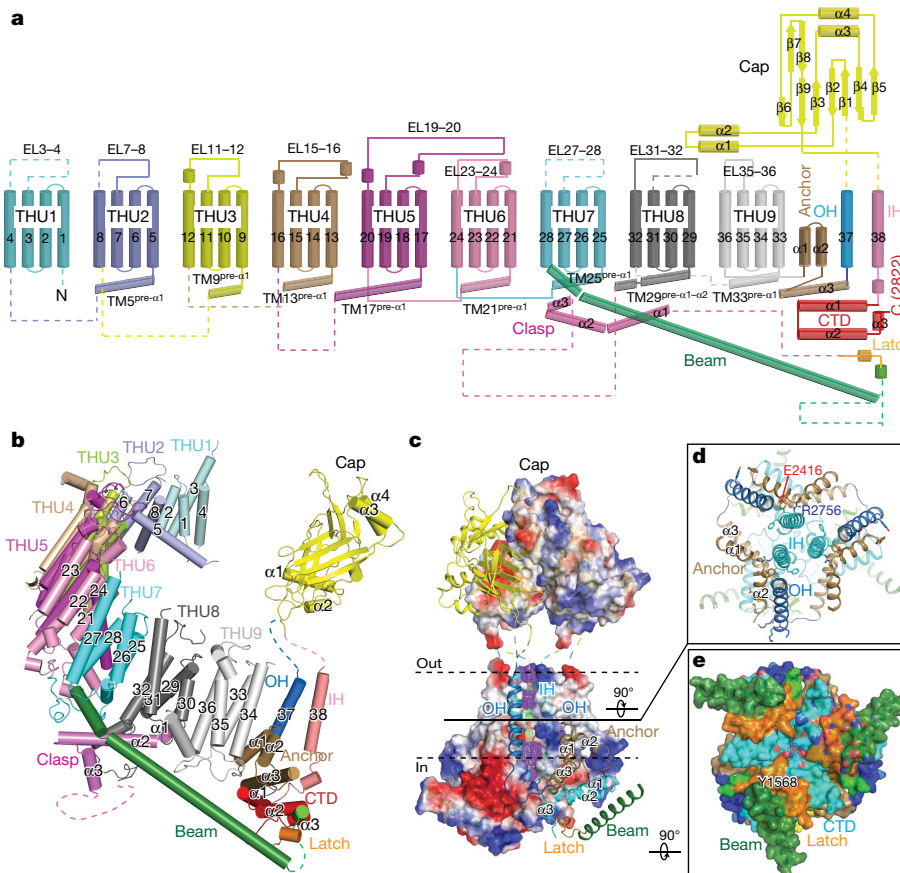


Fig. 2 | The 38-transmembrane-helix topological organization. **a, b**, The 38-transmembrane-helix topological model (**a**) and the structural model (**b**) of a PIEZO2 protomer. Dashed lines indicate unresolved regions. EL, extracellular loop; EL3–4 denotes the extracellular loop that connects TM3 and TM4 (or equivalent for EL7–8, EL11–12 and so on); IH, inner helix; OH, outer helix; pre- α , membrane-parallel α -helix that precedes the THU. **c**, Side view of the trimeric central region. Two subunits are presented as views of the surface electrostatic potential, and the other subunit is shown

the PIEZO2 structure in GDN (Extended Data Fig. 7a–d). Compared to PIEZO2, the three PIEZO1 structures show apparent displacement of the cap, distal blade and beam domains (Extended Data Fig. 7a–c). Notably, the transmembrane gate—but not the cytosolic constriction neck—is dilated in all three PIEZO1 structures (Extended Data Fig. 7d), which suggests that the distinct conformational states of the transmembrane pore between the PIEZO1 and PIEZO2 structures are unlikely to be caused by the use of different detergents. Indeed, dilation of the upper transmembrane gate L2469 of PIEZO1 is closely correlated with the displacement of the cap domain among the three PIEZO1 structures (Extended Data Fig. 7a–d).

As the previously characterized PIEZO1 structure¹⁸ with PDB accession 6B3R (PIEZO1 (PDB: 6B3R)) was determined using similar detergents and cryo-EM sample preparation procedures to those that we used here for PIEZO2, we compared these two structures in detail (Figs. 3, 4, Extended Data Fig. 8). The cap domain of PIEZO1 twists in a clockwise direction relative to PIEZO2 (Fig. 4a, Extended Data Fig. 8a). The outer portion of the inner helix and outer helix, as well as the upper transmembrane gate of PIEZO1, show an apparent outward expansion in a clockwise direction relative to PIEZO2, whereas the neighbouring TM25–TM36 show relatively subtle and anticlockwise motion (Fig. 4b, Extended Data Fig. 8c). Similar changes in the inner helix and the upper transmembrane gate were observed when only the inner helix and the following C-terminal domain were superimposed (Fig. 3d). Relative to PIEZO2, the outer portion of the inner helix of PIEZO1 has an outward expansion of about a helical width (around 5.3 Å) (Fig. 3d). These changes result in an expansion of the upper

in ribbon representation. The central solvent-accessible pathway is marked with a dotted mesh (purple, green and red) generated by the program HOLE. **d**, Ribbon representation of a top-down section from **c**, showing the indicated domains. Residue E2416 (red arrow) in the anchor domain has previously been reported to affect ion-permeation properties³¹. **e**, Bottom views of the trimeric central region in surface representation. The central purple dots indicate the constricted intracellular exit of the central pore.

gate from a radius of 0.9 Å for L2743 in PIEZO2 to a radius of 4.5 Å for L2469 in PIEZO1 (Fig. 3c, e). V2750 of PIEZO2 shows an outward displacement associated with the slight displacement of the main chain, leading to an increase in the radius from 1.4 Å for this position in PIEZO2 to 2.4 Å for the corresponding V2476 in PIEZO1 (Fig. 3c, f).

At the lower transmembrane gate, the bulky benzyl group of the F2754 residue in PIEZO2 cuts into the transmembrane pore and blocks the ion-conducting pathway of PIEZO2 (Figs. 3g, 4c). The benzyl group of the corresponding F2480 residue in PIEZO1 is rotated away from the central axis, which results in an expansion of the pore radius from 0.6 Å at this position in PIEZO2 to 4.0 Å in PIEZO1 (Figs. 3c, g, 4c). Notably, F2754 in PIEZO2 (F2480 in PIEZO1) might form a cation–π interaction with K2753 in PIEZO2 (K2479 in PIEZO1) from the neighbouring subunit (Fig. 3g). PIEZO2(K2753) (or PIEZO1(K2479)) appears to move along with the main chain, which might cause the rotation of the side chain of the neighbouring PIEZO2(F2754) (or PIEZO1(F2480)) (Figs. 3g, 4c). The three PIEZO2(E2757) residues form a constriction with a radius of less than 1 Å in the closed state (Fig. 3b, c, h). The corresponding residue in PIEZO1 is G2483 (Fig. 3a, h), with a pore radius of around 5 Å at this position. Of note, the PIEZO1(E2487) residue that is located one helical turn below is in a dilated position relative to PIEZO2(E2757) (Fig. 3h). The cytosolic constriction neck of PIEZO1(M2493/P2536/E2537) and that of PIEZO2(M2767/P2810/E2811) are largely superimposed in a constricted state (Fig. 3i).

Notably, the domains that surround the lower transmembrane gate—including the anchor domain, outer helix and TM33–TM36—appear to move laterally as a whole in an anticlockwise manner (Fig. 4c, Extended

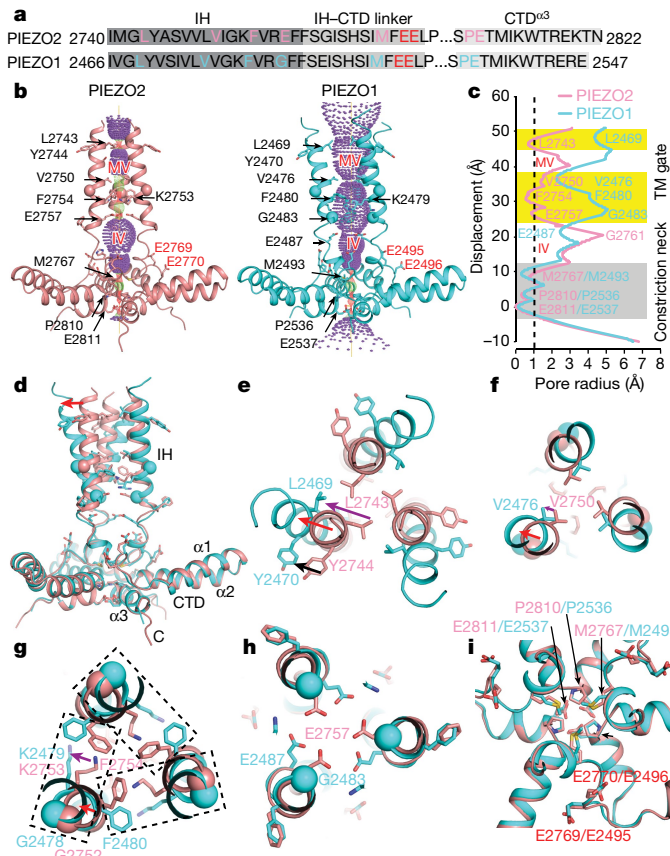


Fig. 3 | The ion-conducting pore. **a**, Sequence alignment between PIEZO1 and PIEZO2 for the inner helix-CTD region. Residues shown in salmon and cyan represent residues that form the transmembrane gate and cytosolic constriction neck; those in red are lateral portal-lining residues. **b**, Ribbon diagram showing the central pore of PIEZO2 (salmon) and that of the previously characterized PIEZO1 (PDB: 6B3R) structure¹⁸ (cyan). The coloured residues shown in **a** are labelled. The central solvent-accessible pathway is marked with a dotted mesh (purple, green and red) generated by the program HOLE (pore radius: red, <1 Å; green, <2 Å; purple, >2 Å). IV, intracellular vestibule; MV, membrane vestibule. **c**, Pore radius along the central axis of the ion-conduction pathway. TM, transmembrane. **d**, Side view of the superimposed PIEZO2 (salmon) and PIEZO1 (cyan) inner helix-CTD. The red arrow indicates the outward shift of the main chain of the inner helix of PIEZO1 relative to that of PIEZO2. **e–i**, Top views of the superimposed PIEZO2 (salmon) and PIEZO1 (cyan) inner helix-CTD, zoomed in near the positions of the indicated residues. Red and purple arrows indicate the position shift of the inner helix main chain or side chain, respectively, of the gate residues of PIEZO1 relative to PIEZO2.

Data Fig. 8d), which is not consistent with the mode of motion of the transmembrane gates. Consistent with the structural analysis, we found that deleting either the whole cap region or the α_1 and α_2 helical domain of the cap ($\text{cap}^{\alpha_1-\alpha_2}$) in either PIEZO1 or PIEZO2 completely abolished whole-cell currents that were evoked by poking—despite the relatively normal expression of these mutant proteins in the plasma membrane (Fig. 4d, Extended Data Fig. 7e–g). Together, these analyses suggest that motion of the cap region might control the opening of the transmembrane gate.

Displacement of cytosolic constriction neck and blade

Compared to PIEZO2, the blade domains of PIEZO1 are curved towards the three-fold central axis, with a graded increase in lateral displacement from THU6 to THU4 (Extended Data Figs. 7b, c, 8a). THU4–THU6 of PIEZO1 also show apparent downward displacement (Extended Data Fig. 8b, e), rendering the transmembrane blade of PIEZO1 flatter than that of PIEZO2 (Extended Data Fig. 8e).

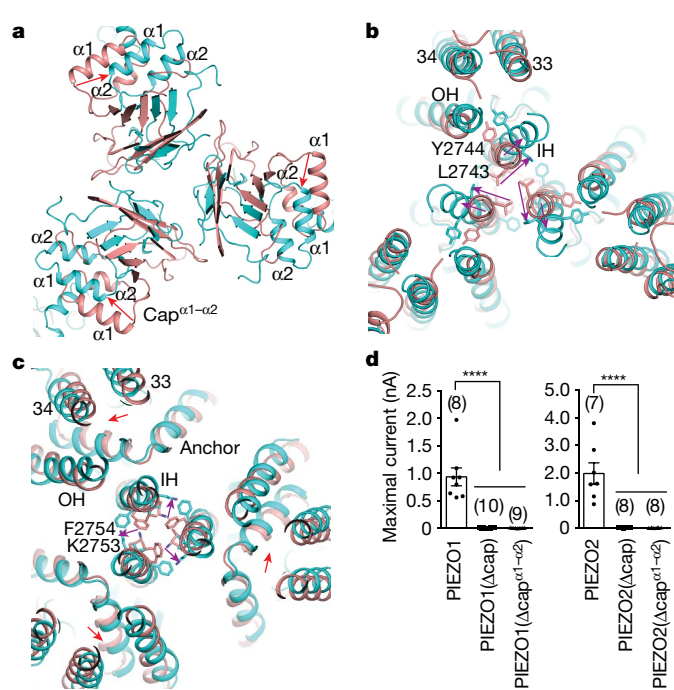


Fig. 4 | Coordinated displacement of the cap domain and the transmembrane gate. **a–c**, Top views of the superimposed PIEZO2 (salmon) and PIEZO1 (PDB: 6B3R) (cyan) structures, zoomed in at $\text{cap}^{\alpha_1-\alpha_2}$ (**a**), the PIEZO2(L2743) residue (**b**), or the PIEZO2(F2754) residue (**c**) (Extended Data Fig. 8a, c, d). Arrows indicate the displacement of PIEZO1 relative to PIEZO2; red arrows show the displacement of the cap or the blade domains; purple arrows show the displacement of the side chains of L2743 or K2753/F2754 in PIEZO2 to the corresponding residues L2469 or K2479/F2480, respectively, in PIEZO1. **d**, Scatter plot of the maximal poking-induced currents. Data are mean \pm s.e.m. and the number of recorded cells is labelled. A one-way analysis of variance (ANOVA) was used for comparisons to either PIEZO1 or PIEZO2; ***P < 0.0001.

The intracellular beam shows an uneven lever-like displacement in which the distal end remains relatively stable, whereas the proximal end shifts both laterally and vertically about a helical width (Extended Data Fig. 8b). This results in a switch from a clockwise and downward displacement of the distal THU4–THU6 (Extended Data Fig. 8a, b) to a collective anticlockwise and upward displacement of the central region (Extended Data Fig. 8b–d, g). Such displacement can lead to an upward displacement of both the cytosolic constriction neck and the transmembrane gate of PIEZO1 relative to those of PIEZO2 (Extended Data Fig. 8f). Furthermore, the three beam domains appear to push the CTDs in an anticlockwise manner, which might twist the constriction neck and cause it to move (Extended Data Fig. 8g). Despite the apparent conformational difference in the beam and the blade domains, the cytosolic constriction neck remains in a constricted state in both PIEZO1 and PIEZO2 (Fig. 3i, Extended Data Fig. 8g).

Discussion

Here we have determined the structure of mouse PIEZO2, with 38 completely resolved transmembrane helices (Figs. 1, 2). Given the sequence homology and structural resemblance between PIEZO2 and PIEZO1, we conclude that PIEZO1 also shares this 38-transmembrane-helix topology. Piezo channels contain 114 transmembrane helices in the trimeric channel complex, which is the largest number that has so far been found among membrane proteins. The transmembrane pore in PIEZO1 is dilated, whereas in PIEZO2 it is closed (Fig. 3). Consequently, we propose that the transmembrane constriction site might act as a transmembrane gate that could be opened by an upward and clockwise motion of the top cap domain (Figs. 3, 4, Extended Data Figs. 7, 8). By contrast, the cytosolic constriction neck remains in a constricted

state in both PIEZO1 and PIEZO2 (Fig. 3), and ascertaining whether this site might function as a cytosolic gate will therefore require further structural and functional evidence. If this is proven to be the case, we hypothesize that the cytosolic gate might be separately gated by the blade and beam structures (Extended Data Figs. 7, 8), indicating a dual-gating mechanism. Consistent with this hypothesis, regions and residues along the pathway between blade and beam have previously been identified to be critical for mechanical and chemical activation of PIEZO1^{16,24}. Furthermore, numerous mutations that cause human disease are clustered at the contacting interfaces between the beam, CTD, outer helix and inner helix (Extended Data Fig. 9). Alternatively, Piezo channels might use the intracellular fenestrations and lateral portals as intracellular ion-conducting routes (Extended Data Fig. 6l, m).

The PIEZO2 structure allows us to evaluate the ‘membrane dome’ and ‘membrane footprint’ hypotheses that have previously been proposed to explain the exquisite mechanosensitivity of Piezo channels^{18,25}. On the basis of the incomplete PIEZO1 structure—with an underestimated mid-plane opening diameter of 18 nm and depth of 6 nm—the membrane dome mechanism predicts the maximal change of the projection area to be about 120 nm² when PIEZO1 becomes completely co-planar with the membrane¹⁸. On the basis of the complete PIEZO2 structure—with a mid-plane opening diameter of 24 nm and a depth of 9 nm (Fig. 1b)—we have calculated the maximal change of the projection area to be around 250 nm², which is more than twice the previous estimation¹⁸. Piezo proteins have also been proposed to deform the membrane shape outside of the perimeter of the channel into a large, curved membrane footprint, which might amplify the mechanosensitivity of the Piezo channels²⁵. As the predicted membrane footprint depends on the actual radius of the Piezo shape, a larger radius of the PIEZO2 structure would make the membrane footprint less prominent. Nevertheless, the dome-shaped Piezo membrane system might potentially allow a much larger change of membrane area than that of the well-characterized bacterial mechanosensitive channel of large conductance (MscL), which has an estimated in-plane membrane expansion of about 20 nm² upon opening^{26–28}. Consistent with this, PIEZO1²⁹ has a measured half-maximal activation tension (T_{50}) of approximately 1.4 mN m⁻¹, whereas MscL^{27,30} has a much larger T_{50} of around 10 mN m⁻¹. It will be interesting to investigate whether the dome shape that is induced by Piezo channels exists in native cell membranes, and whether it might respond to mechanical stimuli for mechanogating.

Online content

Any methods, additional references, Nature Research reporting summaries, source data, extended data, supplementary information, acknowledgements, peer review information; details of author contributions and competing interests; and statements of data and code availability are available at <https://doi.org/10.1038/s41586-019-1505-8>.

Received: 26 March 2019; Accepted: 22 July 2019;

Published online 21 August 2019.

- Coste, B. et al. Piezo1 and Piezo2 are essential components of distinct mechanically activated cation channels. *Science* **330**, 55–60 (2010).
- Coste, B. et al. Piezo proteins are pore-forming subunits of mechanically activated channels. *Nature* **483**, 176–181 (2012).
- Woo, S. H. et al. Piezo2 is required for Merkel-cell mechanotransduction. *Nature* **509**, 622–626 (2014).

- Ranade, S. S. et al. Piezo2 is the major transducer of mechanical forces for touch sensation in mice. *Nature* **516**, 121–125 (2014).
- Chesler, A. T. et al. The role of PIEZO2 in human mechanosensation. *N. Engl. J. Med.* **375**, 1355–1364 (2016).
- Murthy, S. E., Dubin, A. E. & Patapoutian, A. Piezos thrive under pressure: mechanically activated ion channels in health and disease. *Nat. Rev. Mol. Cell Biol.* **18**, 771–783 (2017).
- Szczot, M. et al. PIEZO2 mediates injury-induced tactile pain in mice and humans. *Sci. Transl. Med.* **10**, eaat9892 (2018).
- Murthy, S. E. et al. The mechanosensitive ion channel Piezo2 mediates sensitivity to mechanical pain in mice. *Sci. Transl. Med.* **10**, eaat9897 (2018).
- Woo, S. H. et al. Piezo2 is the principal mechanotransduction channel for proprioception. *Nat. Neurosci.* **18**, 1756–1762 (2015).
- Zhang, M., Wang, Y., Geng, J., Zhou, S. & Xiao, B. Mechanically activated Piezo channels mediate touch and suppress acute mechanical pain response in mice. *Cell Rep.* **26**, 1419–1431 (2019).
- Nonomura, K. et al. Piezo2 senses airway stretch and mediates lung inflation-induced apnoea. *Nature* **541**, 176–181 (2017).
- Zeng, W. Z. et al. PIEZOs mediate neuronal sensing of blood pressure and the baroreceptor reflex. *Science* **362**, 464–467 (2018).
- Coste, B. et al. Gain-of-function mutations in the mechanically activated ion channel PIEZO2 cause a subtype of distal arthrogryposis. *Proc. Natl. Acad. Sci. USA* **110**, 4667–4672 (2013).
- McMillin, M. J. et al. Mutations in PIEZO2 cause Gordon syndrome, Marden-Walker syndrome, and distal arthrogryposis type 5. *Am. J. Hum. Genet.* **94**, 734–744 (2014).
- Ge, J. et al. Architecture of the mammalian mechanosensitive Piezo1 channel. *Nature* **527**, 64–69 (2015).
- Zhao, Q. et al. Structure and mechanogating mechanism of the Piezo1 channel. *Nature* **554**, 487–492 (2018).
- Zhao, Q., Zhou, H., Li, X. & Xiao, B. The mechanosensitive Piezo1 channel: a three-bladed propeller-like structure and a lever-like mechanogating mechanism. *FEBS J.* **286**, 2461–2470 (2019).
- Guo, Y. R. & MacKinnon, R. Structure-based membrane dome mechanism for Piezo mechanosensitivity. *eLife* **6**, e33660 (2017).
- Saotome, K. et al. Structure of the mechanically activated ion channel Piezo1. *Nature* **554**, 481–486 (2018).
- von Heijne, G. Membrane protein structure prediction. Hydrophobicity analysis and the positive-inside rule. *J. Mol. Biol.* **225**, 487–494 (1992).
- Bavi, N. et al. The role of MscL amphipathic N terminus indicates a blueprint for bilayer-mediated gating of mechanosensitive channels. *Nat. Commun.* **7**, 11984 (2016).
- Zhao, Q. et al. Ion permeation and mechanotransduction mechanisms of mechanosensitive Piezo channels. *Neuron* **89**, 1248–1263 (2016).
- Wu, J. et al. Inactivation of mechanically activated Piezo1 ion channels is determined by the C-terminal extracellular domain and the inner pore helix. *Cell Rep.* **21**, 2357–2366 (2017).
- Wang, Y. et al. A lever-like transduction pathway for long-distance chemical- and mechano-gating of the mechanosensitive Piezo1 channel. *Nat. Commun.* **9**, 1300 (2018).
- Haselwandter, C. A. & MacKinnon, R. Piezo’s membrane footprint and its contribution to mechanosensitivity. *eLife* **7**, e41968 (2018).
- Perozo, E., Cortes, D. M., Sompornpisut, P., Kloda, A. & Martinac, B. Open channel structure of MscL and the gating mechanism of mechanosensitive channels. *Nature* **418**, 942–948 (2002).
- Chiang, C. S., Anishkin, A. & Sukharev, S. Gating of the large mechanosensitive channel in situ: estimation of the spatial scale of the transition from channel population responses. *Biophys. J.* **86**, 2846–2861 (2004).
- Chang, G., Spencer, R. H., Lee, A. T., Barclay, M. T. & Rees, D. C. Structure of the MscL homolog from *Mycobacterium tuberculosis*: a gated mechanosensitive ion channel. *Science* **282**, 2220–2226 (1998).
- Lewis, A. H. & Grandi, J. Mechanical sensitivity of Piezo1 ion channels can be tuned by cellular membrane tension. *eLife* **4**, e12088 (2015).
- Cox, C. D. et al. Removal of the mechanoprotective influence of the cytoskeleton reveals PIEZO1 is gated by bilayer tension. *Nat. Commun.* **7**, 10366 (2016).
- Coste, B. et al. Piezo1 ion channel pore properties are dictated by C-terminal region. *Nat. Commun.* **6**, 7223 (2015).

Publisher’s note: Springer Nature remains neutral with regard to jurisdictional claims in published maps and institutional affiliations.

© The Author(s), under exclusive licence to Springer Nature Limited 2019

METHODS

Data reporting. No statistical methods were used to predetermine sample size. The experiments were not randomized and the investigators were not blinded to allocation during experiments and outcome assessment.

Molecular cloning. We thank A. Patapoutian at Scripps Research for sharing the mouse *Piezo2* cDNA. *Piezo2* was sub-cloned into the pcDNA3.1 expression vector encoding a C-terminal glutathione S-transferase (GST) tag with a precision protease cleavage site in between, followed by the GFP-coding sequence driven by an internal ribosome entry site (IRES) (for monitoring the efficiency of transient transfection and protein expression). We refer to this expression plasmid as PIEZO2-pp-GST-IRES-GFP (Extended Data Fig. 1a). When PIEZO1-KO-HEK cells (in which the endogenous *PIEZO1* gene is disrupted)³² were transfected with this plasmid and assayed with a piezoelectrically driven glass probe to indent the cell membrane, similar whole-cell currents were evoked by poking to cells that were transfected with a PIEZO2-IRES-GFP vector (Extended Data Fig. 1b–d)—suggesting that fusion of GST at the C terminus of PIEZO2 did not affect its functionality. All constructs including PIEZO2(E2757A)-mRuby2, PIEZO2(E2811A)-mRuby2, PIEZO1(E2537A)-mRuby2, PIEZO1(Δ cap^{α1-α2})-GST (in which residues 2253–2274 were replaced with a GGGGG linker), PIEZO2(Δ cap)-mRuby2 (in which residues 2502–2727 were replaced with a GGGG linker) and PIEZO2(Δ cap^{α1-α2})-mRuby2 (in which residues 2536–2557 were replaced with a GGGG linker) were sub-cloned using the One Step Cloning Kit (Vazyme Biotech) according to the instruction manual and as previously described²², then sequenced to validate the desired mutations.

Protein expression and purification of PIEZO2. The purification procedure of the PIEZO2 protein was adapted from the previously described protocol for purification of PIEZO1, with substantial modifications¹⁶. Owing to the much lower expression level of PIEZO2 than PIEZO1 (Extended Data Fig. 1e), we scaled up to 120 15-cm Petri dishes for culture and transfection of HEK293T cells to obtain around 50 µg of purified PIEZO2 proteins suitable for each cryo-EM experiment trial, following the purification procedure described below (Extended Data Fig. 1g, h). Furthermore, on the basis of fast protein liquid chromatography gel filtration and negative-staining electron microscopy (Extended Data Fig. 1f–i), we found that the detergent GDN, which is a synthetic substitute of digitonin and was used for determining the PIEZO1 (PDB: 6BPZ) structure¹⁹, was more suitable for PIEZO2 proteins than the detergent C₁₂E₁₀ that was used for determining the previous PIEZO1 (PDB: 5Z10) structure¹⁶.

For each batch of protein purification, transiently transfected HEK293T cells cultured in 120 150 × 25-mm Petri dishes with a total of 2.4 l of culture medium were collected by centrifugation at 850g and solubilized in buffer A, containing 25 mM NaPIPES pH 7.3, 150 mM NaCl, 3 mM dithiothreitol (DTT), a mixture of detergents including 0.012% (w/v) GDN, 0.1% (w/v) C₁₂E₆, 1% (w/v) CHAPS, 0.5% (w/v) L- α -phosphatidylcholine (Avanti), a cocktail of protease inhibitors (Roche) and 3 mM phenylmethylsulfonyl fluoride (PMSF) at 4°C for 1.5 h. After centrifugation at 13,000g for 35 min, the supernatant was collected and incubated with glutathione sepharose beads (GE Healthcare) at 4°C for 7 h. The resin was washed extensively with buffer B, containing 25 mM Na-PIPES pH 7.3, 150 mM NaCl, 3 mM DTT and 0.05% (w/v) GDN. The GST-tagged PIEZO2 was cleaved off by PreScission Protease (GE Healthcare) in buffer B at 4°C for 16 h, and subjected to size-exclusion chromatography (Superose-6 10/300 GL, GE Healthcare) in buffer C, containing 25 mM Na-PIPES pH 7.3, 150 mM NaCl, 3 mM DTT and 0.02% (w/v) GDN. Peak fractions representing oligomeric PIEZO2 were collected for electron microscopy analysis. The protein in GDN was used for final cryo-EM structure determination. All detergents used in this project were purchased from Anatrace.

Negative-staining electron microscopy. An aliquot of 4 µl PIEZO2 (0.03 mg ml⁻¹) was applied to 15-s glow-discharged carbon-coated copper grids (300 mesh, Zhongjingkeyi Technology). After the grids were incubated at room temperature for 1 min, excess liquid was absorbed by filter paper. Grids containing the specimen were stained by applying droplets of 2% uranyl acetate for 30 s and air-dried. Micrographs were collected on a T12 microscope (FEI) operated at 120 kV, using a 4k × 4k CCD camera (UltraScan 4000, Gatan). Images were recorded at a nominal magnification of 49,000 \times .

Sample preparation and cryo-EM data acquisition. The sample preparation procedure was optimized by following previously described protocols^{18,33} so that the PIEZO2 proteins at a concentration of approximately 1 mg ml⁻¹ could enter into the holes without a thin carbon film for absorbing and concentrating the proteins, which might reduce the background noise and improve the image quality. In brief, 3 µl of freshly purified mouse PIEZO2 proteins (around 1 mg ml⁻¹) each time were sequentially blotted 3 times to 300-mesh holey carbon Au R2/1 grids treated with 25 s of glow discharge (Quantifoil, Micro Tools GmbH). Fluorinated Fos-choline-8 (0.65 mM; Hampton) was added to the freshly concentrated PIEZO2 sample immediately before freezing. The grids were then blotted and plunged into liquid ethane using an FEI Mark IV Vitrobot operated at 8°C and 100% humidity.

The grids were transferred to a 300 kV Titan Krios (FEI) electron microscope equipped with a Cs corrector and GIF Quantum energy filter (slit width 20 eV). Images were recorded by a post-GIF K2 Summit direct electron detector (Gatan) working at the super-resolution mode. Data acquisition was performed using AutoEMation II with a nominal magnification of 81,000 \times , which yields a super-resolution pixel size of 0.7005 Å on the image plane, and with defocus ranging from -1.5 to -2.5 µm. The dose rate on the detector was around 8.4 counts per physical pixel per second with a frame exposure time of 0.275 s and a total exposure time of 8.8 s. Each micrograph stack contains 32 frames. The total dose was approximately 50 e⁻ per Å² for each micrograph.

Image processing. A simplified flowchart of the procedure for image processing is presented in Extended Data Fig. 3. Three batches of cryo-EM data containing 8,792, 8,621 and 5,661 micrograph stacks, respectively, were processed in the first few steps. The stacks were motion-corrected and dose-weighted using MotionCor2³⁴ with 2 × 2 binning, resulting in a pixel size of 1.401 Å. After whole-image CTF estimation using CTFFIND3³⁵, 7,243, 7,685 and 4,915 good micrographs, respectively, were manually selected. A total of 1,260,085, 948,941 and 512,933 particles, respectively, were auto-picked using RELION-3.0³⁶. After several rounds of 2D classification, 184, 226, 271,730 and 178,808 particles, respectively, were selected and subjected to 3D refinement. The PIEZO1 electron microscopy map (EMD-6865), low-pass-filtered to 60 Å, was used as an initial model. Each particle was re-centred and subjected to Gett³⁷ to refine the local defocus parameters. The well-centred particles with more accurate defocus parameters were re-extracted from the motion-corrected and dose-weighted micrographs and subjected to 3D refinement, which resulted in three electron density maps at 6.23 Å, 4.82 Å and 5.15 Å resolution.

A total of 634,764 particles selected from the three datasets were pooled for further processing. Three parallel 3D classifications skipping alignment were performed with three, four and five classes, respectively. Particles from each class (or from the merging of several classes that had similar density maps) were subjected to 3D refinement, separately, resulting in multiple density maps. These density maps were thoroughly compared and the maps with the highest resolution in each classification showed nearly the same structures, indicating that they might represent a similar conformation of PIEZO2. Particles from these highest-resolution classes were merged to yield a dataset with 281,283 particles. All duplicated particles derived from the parallel routine of 3D classifications and 3D refinements were removed during data merging. After 3D refinement, this dataset yielded a map at 4.15 Å resolution. To further improve the resolution, random phase classification was used to remove heterogeneous particles, and this resulted in a new map at 3.80 Å resolution after 3D refinement and post-processing. All 3D refinement and 3D classification above except random phase classification were performed with C₃ symmetry.

As the cap domain and the distal blade were absent from the overall 3.80 Å map, focused refinements were performed for these regions. The subroutine of relion_particle_symmetry_expand in RELION-3.0 was used to expand 281,283 PIEZO2 particles with C₃ symmetry. Then 843,849 blade particles were obtained using the subtraction of two adjacent blades in raw images. These blade particles were subjected to 3D refinement, resulting in a focused map of 3.83 Å resolution. After further 3D classification with a local angular search of 0.9° step size and 5° search range, 386,144 particles were selected and subjected to 3D refinement, resulting in the final focused map of the blade at 3.64 Å resolution. As the density of THU1 was still fragmentary and unclear in this map, more surrounding regions of the distal blade were subtracted from the 386,144 blade particles, and the following focused refinement led to a reconstruction at 3.93 Å resolution. After a 3D classification skipping alignment, 347,108 particles were further selected from the 386,144 particles and subjected to 3D refinement, yielding the final focused map of the distal blade at 3.77 Å resolution.

In another processing, a focused refinement of the central region of the 281,283 particles was performed by subtracting the projections of most parts of three surrounding blades. C₃ symmetry was imposed during the refinement and resulted in a focused map at 3.80 Å resolution. As the density of the cap domain was still fragmentary and unclear in this map, 3D classification skipping alignment with a local mask of the cap domain was performed. A total of 108,781 particles from the class with the best density of cap domain were selected and subjected to 3D refinement with a soft mask of the central region, resulting in the final focused map of the central region at 3.86 Å resolution. The three final focused maps were fit together according to their overlapping area using Chimera³⁸, then combined using PHENIX combine_focused_maps. Three copies of the combined map were further combined into the final density map.

The reported resolutions are based on the gold-standard Fourier shell correlation 0.143 criterion³⁹. All density maps were sharpened by applying a negative B-factor that was estimated using automated procedures⁴⁰. Variations in local resolution were estimated using Resmap⁴¹.

Model building and structure refinement. The cryo-EM structures of PIEZO1 (PDB: 5Z10 and 6B3R) and the crystal structure of the PIEZO1 cap domain (PDB: 4RAX) were docked into the cryo-EM map in Chimera as the initial models. The structure was first refined in real space using PHENIX with secondary structure and non-crystallographic symmetry restraints. The model of THU1–THU3 was built de novo in Coot⁴². The remaining part of the model was manually mutated from refined initial models. Four N-acetylglucosamine groups were modelled onto residues N769, N1030, N1037 and N2642 as N-linked glycosylation (Extended Data Fig. 4). Some lipid-like density was observed, but not modelled owing to potential ambiguity. Compared to the full-length 2,547-residue mouse PIEZO1, the 2,822-residue mouse PIEZO2 has 275 extra residues, which are mainly located in the structurally unresolved loop regions (Supplementary Table 1). The model was refined in real space using PHENIX⁴³ with secondary structure and non-crystallographic symmetry restraints. The final atomic model was evaluated using MolProbity⁴⁴.

Western blotting. Western blotting was carried out as previously described¹⁸. In brief, 1 150-mm Petri dish of HEK293T cells transfected with vector, mouse PIEZO1-pp-GST-IRES-GFP or mouse PIEZO2-pp-GST-IRES-GFP were collected and lysed into 700-μl cell lysates. Around 10 μl of cell lysate from each sample was separated on 8% SDS-PAGE gels and transferred onto 0.45-μm PVDF membranes (Millipore). The membranes were blocked by 5% non-fat milk (Bio-Rad) in TBST buffer (TBS buffer with 0.1% Tween-20) and incubated with the diluted primary antibodies overnight. After three washes with TBST buffer, the membranes were incubated with the peroxidase-conjugated anti-rabbit IgG secondary antibody (Cell Signaling Technology, 1:10,000) at room temperature for 1 h, followed by washing and detection using an enhanced chemiluminescence detection kit (Thermo Fisher Scientific). The antibodies used for western blotting included rabbit anti-GST (Millipore, 1:3,000) and rabbit anti-β-actin (Cell Signaling Technology, 1:3,000).

Cell-surface biotinylation assay. To examine the plasma-membrane expression of PIEZO1-GST, PIEZO1(Δcap)-GST, PIEZO1(Δcap^{α1-α2})-GST, PIEZO2-mRuby2 and PIEZO2(Δcap^{α1-α2})-mRuby2, a cell-surface biotinylation assay was carried out according to the procedure previously described⁴⁵. The anti-GST antibody (Millipore, 1:3,000) was used for detecting the PIEZO1-GST, PIEZO1(Δcap)-GST and PIEZO1(Δcap^{α1-α2})-GST fusion proteins, and a custom-generated PIEZO2 antibody (1:1,000) using the synthesized peptide NH₂-KAPSDNSKPIKQC-CONH₂ (which corresponds to residues 2662–2674 in the cap of mouse PIEZO2) was used for detecting the PIEZO2-mRuby2 and PIEZO2(Δcap^{α1-α2})-mRuby2 fusion proteins. The PIEZO2 antibody did not recognize protein bands from the vector-transfected cells (Extended Data Fig. 7f) and the PIEZO2(Δcap) protein (data not shown), demonstrated the specificity of the PIEZO2 antibody in recognizing the PIEZO2 proteins in western blotting. To detect the PIEZO2(Δcap)-mRuby2 protein (Extended Data Fig. 7g), the anti-Flag antibody (Sigma, 1:3,000) was used to detect the Flag epitope located in the C terminus of the PIEZO2-mRuby2 or PIEZO2(Δcap)-mRuby2 fusion proteins. The anti-rabbit IgG (CST, 1:10,000) or anti-mouse IgG (Pierce, 1:20,000) secondary antibodies were used.

Whole-cell electrophysiology and mechanical stimulation. The protocols for culture of PIEZO1-KO-HEK cells in which the endogenous *PIEZO1* gene is disrupted³², transient transfection and patch-clamp experiments with an Axopatch 200B amplifier (Axon Instruments) or HEKA EPC10 were essentially similar to those previously described, except that polyethylenimine (PEI) (Polysciences) was used for the transfection reagent^{16,22}. For whole-cell patch-clamp recordings, the recording electrodes had a resistance of 2–5 MΩ when filled with an internal solution composed of 133 mM CsCl, 1 mM CaCl₂, 1 mM MgCl₂, 5 mM EGTA, 10 mM HEPES (pH 7.3 with CsOH), 4 mM MgATP and 0.4 mM Na₂GTP. The extracellular solution was composed of 133 mM NaCl, 3 mM KCl, 2.5 mM CaCl₂, 1 mM MgCl₂, 10 mM HEPES (pH 7.3 with NaOH) and 10 mM glucose. All experiments were carried out at room temperature. The currents were sampled at 20 kHz and filtered at 2 kHz using Clampex 10.4 software (Axon Instruments) or Patchmaster software. Leak currents before mechanical stimulation were subtracted off-line from the current traces.

Mechanical stimulation was delivered to the cell during the patch-clamp recording at an angle of 80° using a fire-polished glass pipette (tip diameter 3–4 μm) as previously described^{1,2}. The downward movement of the probe towards the cell was driven by a Clampex-controlled piezoelectric crystal micro-stage (E625 LVPZT Controller/Amplifier; Physik Instrument). The probe had a velocity of 1 μm ms⁻¹ during the downward and upward motion, and the stimulus was maintained for 150 ms. A series of mechanical steps in 1-μm increments was applied every 8 s and the currents were recorded at a holding potential of -80 mV.

Measurement of P_{Ca}/P_{Cs} . The measurements were carried out as previously described^{22,31}. In brief, P_{Ca}/P_{Cs} was measured in the internal solution consisting of 149 mM caesium methanesulfonate, 1 mM CsCl and 10 mM HEPES (pH 7.3 with CsOH) and the extracellular solution containing 50 mM calcium gluconate, 0.5 mM CaCl₂, 10 mM HEPES and 170 mM sucrose (pH 7.3 with

CsOH). For *I*–*V* relationship recordings, voltage steps were applied 700 ms before mechanical stimulation (150 ms) from a holding potential of -60 mV. Voltage steps were given from -37.1 mV to 22.9 mV in 10-mV increments (the liquid junction potential of 7.1 mV was corrected). The reversal potential for each cell under the specific recording solution was determined by linear regression fit of the whole-cell *I*–*V* curve. Permeability ratios were calculated by using the following, previously described³¹ Goldman–Hodgkin–Katz equation (in which E_{rev} is the reversal potential, R is the universal gas constant, T is the absolute temperature and F is Faraday's constant):

$$\frac{P_{Ca}}{P_{Cs}} : E_{rev} = \frac{RT}{F} \ln \left(\sqrt{\frac{4P_{Ca} [Ca]_o}{P_{Cs} [Cs]_i}} + \frac{1}{4} - \frac{1}{2} \right)$$

Measurement of unitary conductance. Single-channel currents were recorded in the cell-attached patch-clamp configuration using HEKA EPC10 as previously described^{1,22}. Currents were sampled at 20 kHz and filtered at 1 kHz. The recording electrodes had a resistance of 2–3 MΩ when filled with standard solution containing 130 mM NaCl, 5 mM KCl, 1 mM CaCl₂, 1 mM MgCl₂, 10 mM TEA-Cl and 10 mM HEPES (pH 7.3 with NaOH). The external solution used to zero the membrane potential consisted of 140 mM KCl, 1 mM MgCl₂, 10 mM glucose and 10 mM HEPES (pH 7.3 with KOH). Membrane patches were stimulated with 500-ms negative-pressure pulses through the recording electrode using a Patchmaster controlled pressure clamp HSPC-1 device (ALA Scientific). In contrast to PIEZO1, PIEZO2 is reported to be insensitive to stretch simulation⁴⁶. Indeed, in our studies, compared to the near-100% stretch responsiveness of PIEZO1-expressing cells, only about 25% of PIEZO2-expressing cells (16 out of 62) generated stretch-activated currents (Extended Data Fig. 6g), despite PIEZO1- and PIEZO2-expressing cells mediating poking-evoked whole-cell currents to a similar level (Fig. 4d). Recordings with one to four channel openings were generally used. Single-channel amplitude at a given potential was measured from trace histograms of 10–80 repeated recordings. Histograms were fitted with Gaussian equations using either the Clampfit 10 software or multi-peak fitting analysis of the Origin Pro software. The single-channel slope conductance for each individual cell was calculated from a linear regression curve fit to single-channel *I*–*V* plots.

Reporting summary. Further information on research design is available in the Nature Research Reporting Summary linked to this article.

Data availability

The structural coordinates of mouse PIEZO2 have been deposited in the PDB under the accession 6KG7. The cryo-EM map was deposited into the Electron Microscopy Data Bank (EMDB) under the accession 9975.

32. Lukacs, V. et al. Impaired PIEZO1 function in patients with a novel autosomal recessive congenital lymphatic dysplasia. *Nat. Commun.* **6**, 8329 (2015).
33. Lü, W., Du, J., Goehring, A. & Gouaux, E. Cryo-EM structures of the trimeric NMDA receptor and its allosteric modulation. *Science* **355**, eaal3729 (2017).
34. Zheng, S. Q. et al. MotionCor2: anisotropic correction of beam-induced motion for improved cryo-electron microscopy. *Nat. Methods* **14**, 331–332 (2017).
35. Mindell, J. A. & Grigorieff, N. Accurate determination of local defocus and specimen tilt in electron microscopy. *J. Struct. Biol.* **142**, 334–347 (2003).
36. Zivanov, J. et al. New tools for automated high-resolution cryo-EM structure determination in RELION-3. *eLife* **7**, e42166 (2018).
37. Zhang, K. Gctf: Real-time CTF determination and correction. *J. Struct. Biol.* **193**, 1–12 (2016).
38. Pettersen, E. F. et al. UCSF Chimera—a visualization system for exploratory research and analysis. *J. Comput. Chem.* **25**, 1605–1612 (2004).
39. Scheres, S. H. & Chen, S. Prevention of overfitting in cryo-EM structure determination. *Nat. Methods* **9**, 853–854 (2012).
40. Rosenthal, P. B. & Henderson, R. Optimal determination of particle orientation, absolute hand, and contrast loss in single-particle electron cryomicroscopy. *J. Mol. Biol.* **333**, 721–745 (2003).
41. Kucukelbir, A., Sigworth, F. J. & Tagare, H. D. Quantifying the local resolution of cryo-EM density maps. *Nat. Methods* **11**, 63–65 (2014).
42. Emsley, P., Lohkamp, B., Scott, W. G. & Cowtan, K. Features and development of Coot. *Acta Crystallogr. D* **66**, 486–501 (2010).
43. Adams, P. D. et al. PHENIX: a comprehensive Python-based system for macromolecular structure solution. *Acta Crystallogr. D* **66**, 213–221 (2010).
44. Chen, V. B. et al. MolProbity: all-atom structure validation for macromolecular crystallography. *Acta Crystallogr. D* **66**, 12–21 (2010).
45. Zhang, T., Chi, S., Jiang, F., Zhao, Q. & Xiao, B. A protein interaction mechanism for suppressing the mechanosensitive Piezo channels. *Nat. Commun.* **8**, 1797 (2017).
46. Moroni, M., Servin-Vences, M. R., Fleischer, R., Sánchez-Carranza, O. & Lewin, G. R. Voltage gating of mechanosensitive PIEZO channels. *Nat. Commun.* **9**, 1096 (2018).

Acknowledgements We thank A. Patapoutian for sharing the mouse *Piezo2* cDNA and the Tsinghua University Branch of the China National Center for

Protein Sciences (Beijing) for providing cryo-EM facility support. This work was supported by grant numbers 2016YFA0500402, 31825014, 31630090 and 2015CB910102 to B.X. and 31570730, 2016YFA0501102 and 2016YFA0501902 to X.L., from either the National Key R&D Program of China or the National Natural Science Foundation of China.

Author contributions L.W. carried out protein purification, electron microscopy sample preparation and data collection; H.Z. performed electron microscopy sample preparation, data collection, image processing and model building; M.Z. did electrophysiology; W.L. did electrophysiology and plasmid preparation; T.D. did mutagenesis; Q.Z. cloned the expression vector and helped with initial testing of expression; Y.L. helped with experiments; L.L. assisted in collection of electron microscopy data; X.L. supervised collection and analysis of electron microscopy data; B.X. conceived and directed the

study, analysed the structure, made the figures and wrote the manuscript with help from all other authors.

Competing interests The authors declare no competing interests.

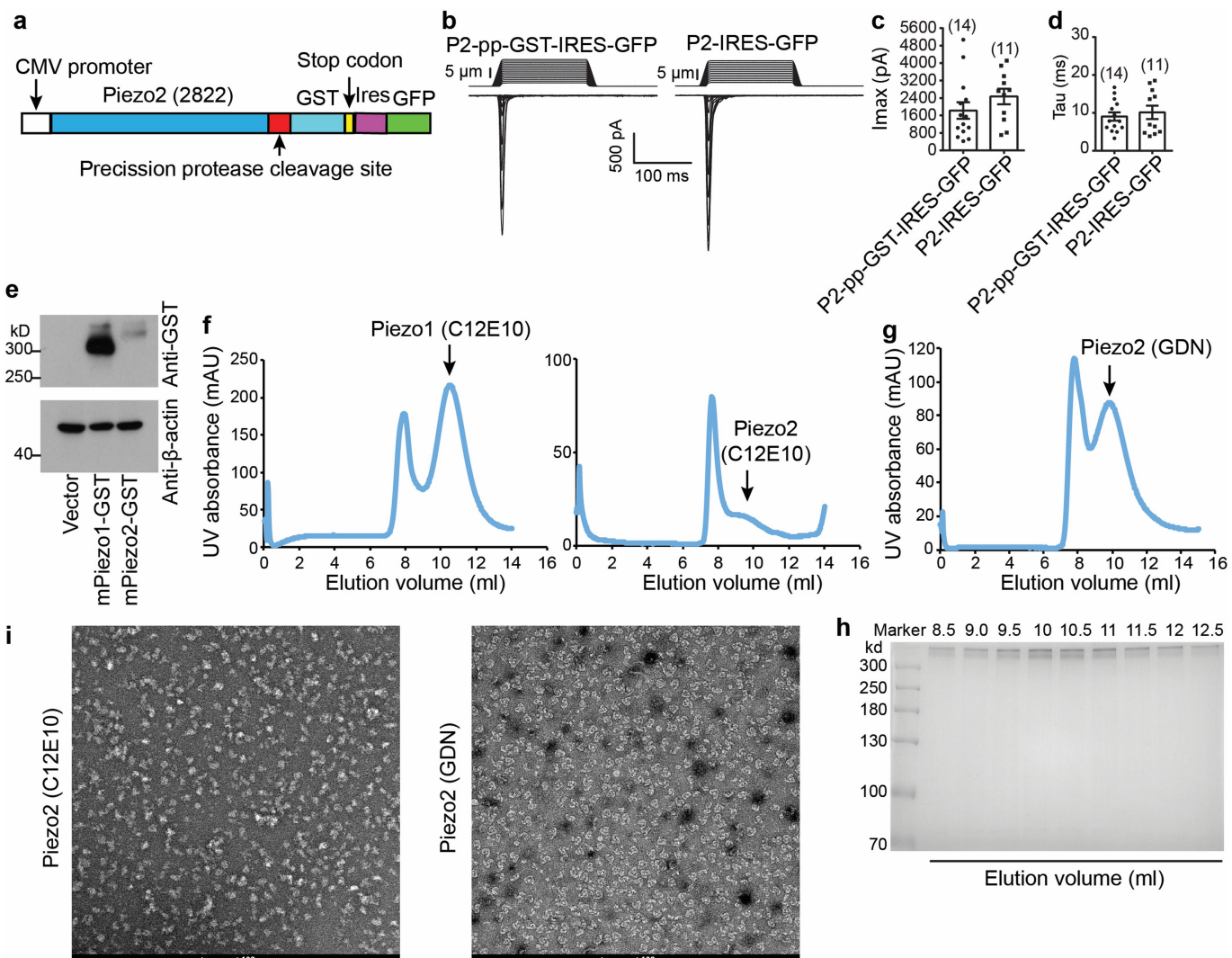
Additional information

Supplementary information is available for this paper at <https://doi.org/10.1038/s41586-019-1505-8>.

Correspondence and requests for materials should be addressed to X.L. or B.X.

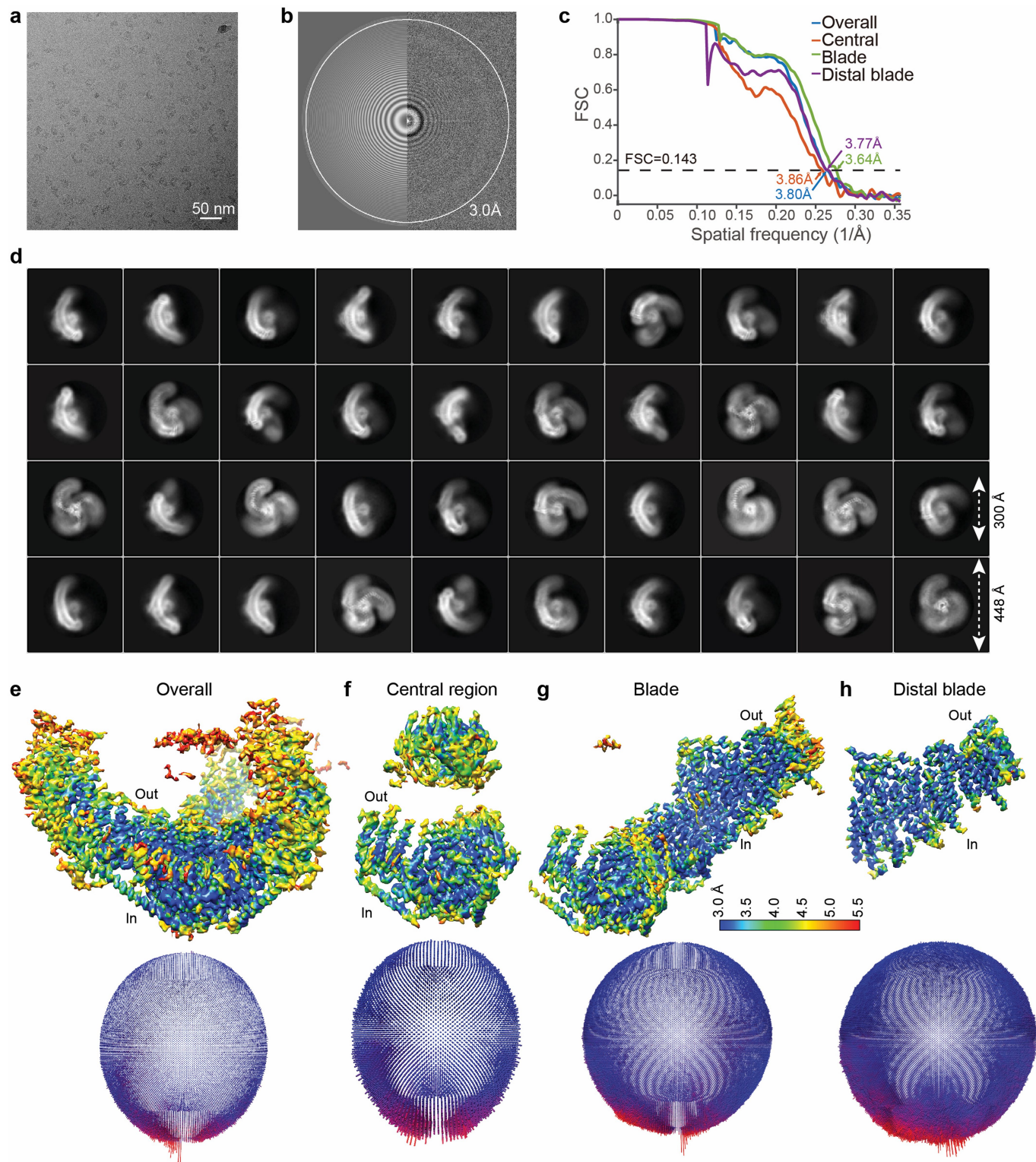
Peer review information *Nature* thanks Boris Martinac, Edwin McCleskey and the other, anonymous, reviewer(s) for their contribution to the peer review of this work.

Reprints and permissions information is available at <http://www.nature.com/reprints>.



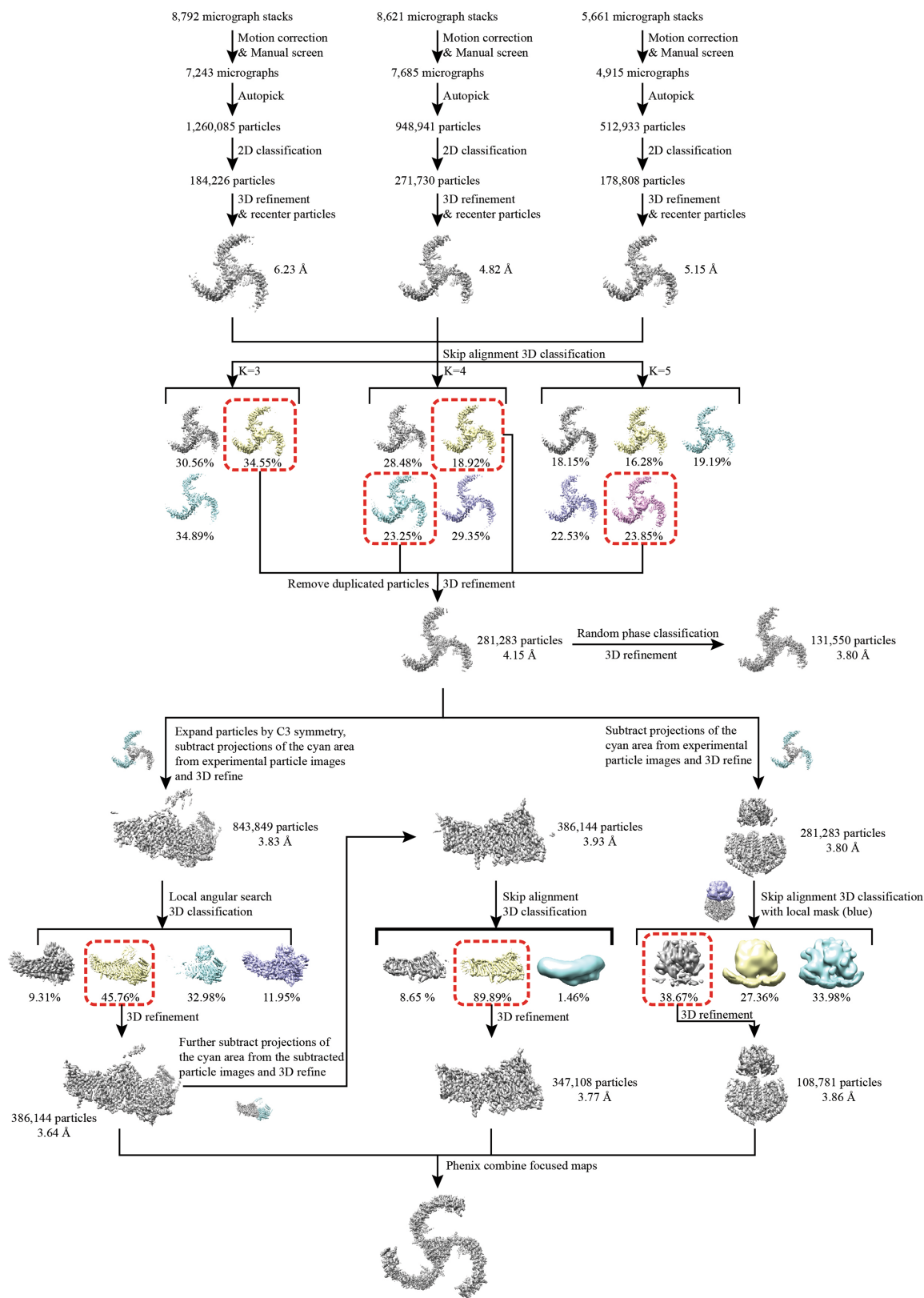
Extended Data Fig. 1 | Optimization of the purification of recombinant PIEZO2 proteins. **a**, Schematic of the PIEZO2-pp-GST-IRES-GFP expression construct driven by the cytomegalovirus (CMV) promoter. **b**, Representative traces of inward currents at -80 mV evoked by a series of mechanically probing steps in $1\text{-}\mu\text{m}$ increments in whole-cell configuration in PIEZO1-KO HEK cells transfected with the indicated constructs. The number of cells recorded is shown in **c**. P2, PIEZO2. **c**, **d**, Scatter plots of the maximal poking-induced currents (I_{\max}) (**c**) and the inactivation τ (**d**). Data are mean \pm s.e.m. and the number of recorded cells is labelled. Two-tailed unpaired Student's *t*-test; $P = 0.2347$ (**c**) and $P = 0.5826$ (**d**). **e**, Western blotting of cell lysates derived from HEK293T cells transfected with the

indicated constructs. The anti-GST antibody detected the PIEZO1-GST and PIEZO2-GST proteins, and the anti- β -actin antibody detected β -actin for a loading control. m indicates a mouse-derived protein. **f**, Representative traces of gel filtration of purified PIEZO1 or PIEZO2 proteins using the detergent C₁₂E₁₀. UV, ultraviolet. **g**, A representative trace of gel filtration of the purified full-length PIEZO2 with the GST affinity tag cleaved, in the detergent GDN. **h**, Coomassie blue staining showing the purified PIEZO2 proteins separated on an 8% SDS-PAGE gel. **i**, Representative negative-staining electron microscopy images of PIEZO2 purified in either C₁₂E₁₀ or GDN. The experiments in **e–i** were independently repeated at least three times with similar results.

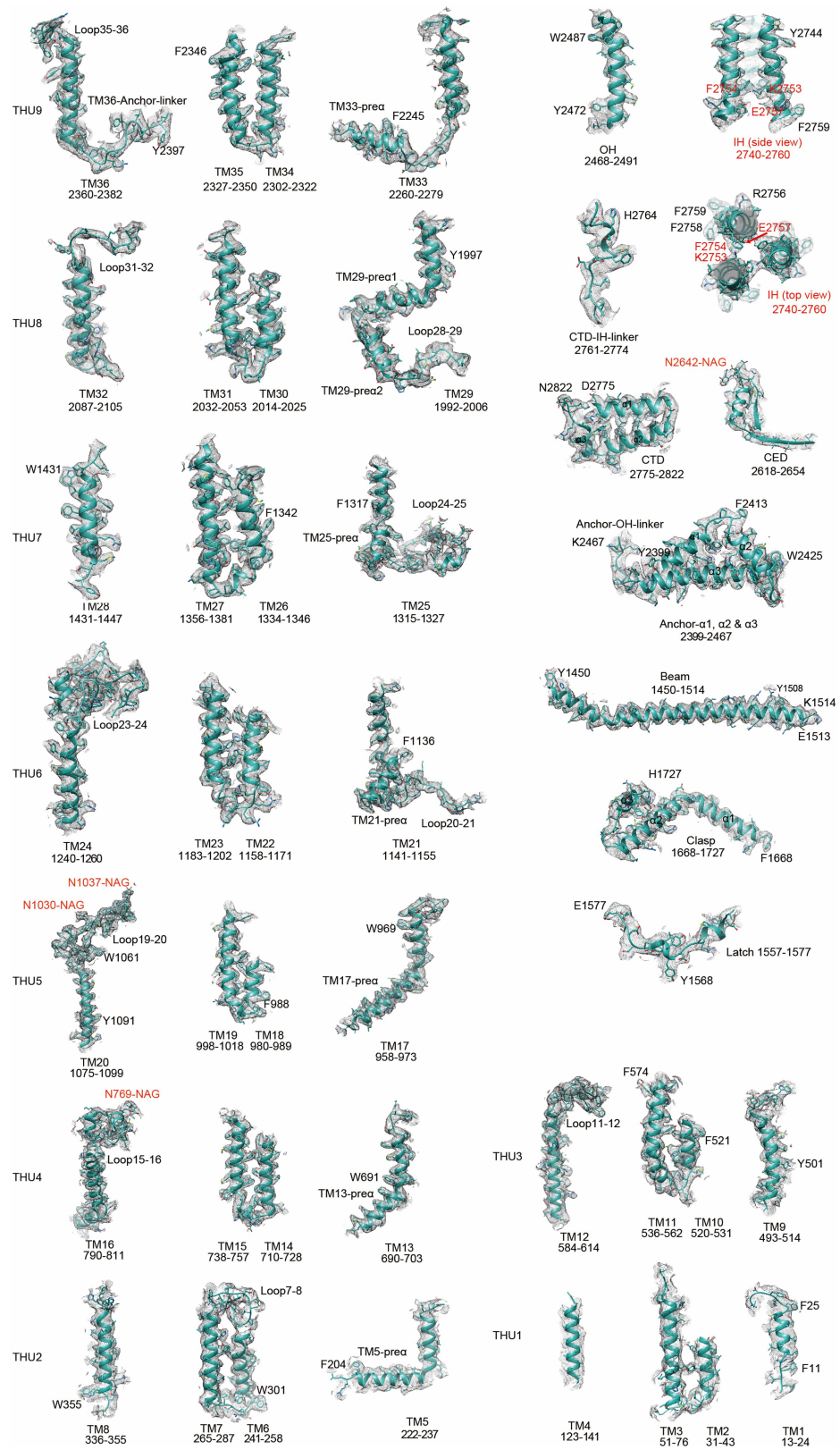


Extended Data Fig. 2 | Determination of the cryo-EM structure of PIEZO2. **a**, Representative cryo-electron micrograph of PIEZO2 solubilized in the detergent GDN. **b**, Power spectrum of the micrograph in **a**, with the 3.0 Å frequency indicated. **c**, Gold-standard Fourier shell correlation (FSC) curves of the indicated density maps. Reported resolutions were based on the FSC = 0.143 criterium. **d**, Representative 2D

class averages of PIEZO2 particles, showing the three-bladed, propeller-like top view and a bowl-like side view. **e–h**, Top, local-resolution maps of the indicated densities. Bottom, Euler angle distribution of particles that were used in the final 3D reconstruction; the height of the cylinder is proportional to the number of particles for that view.

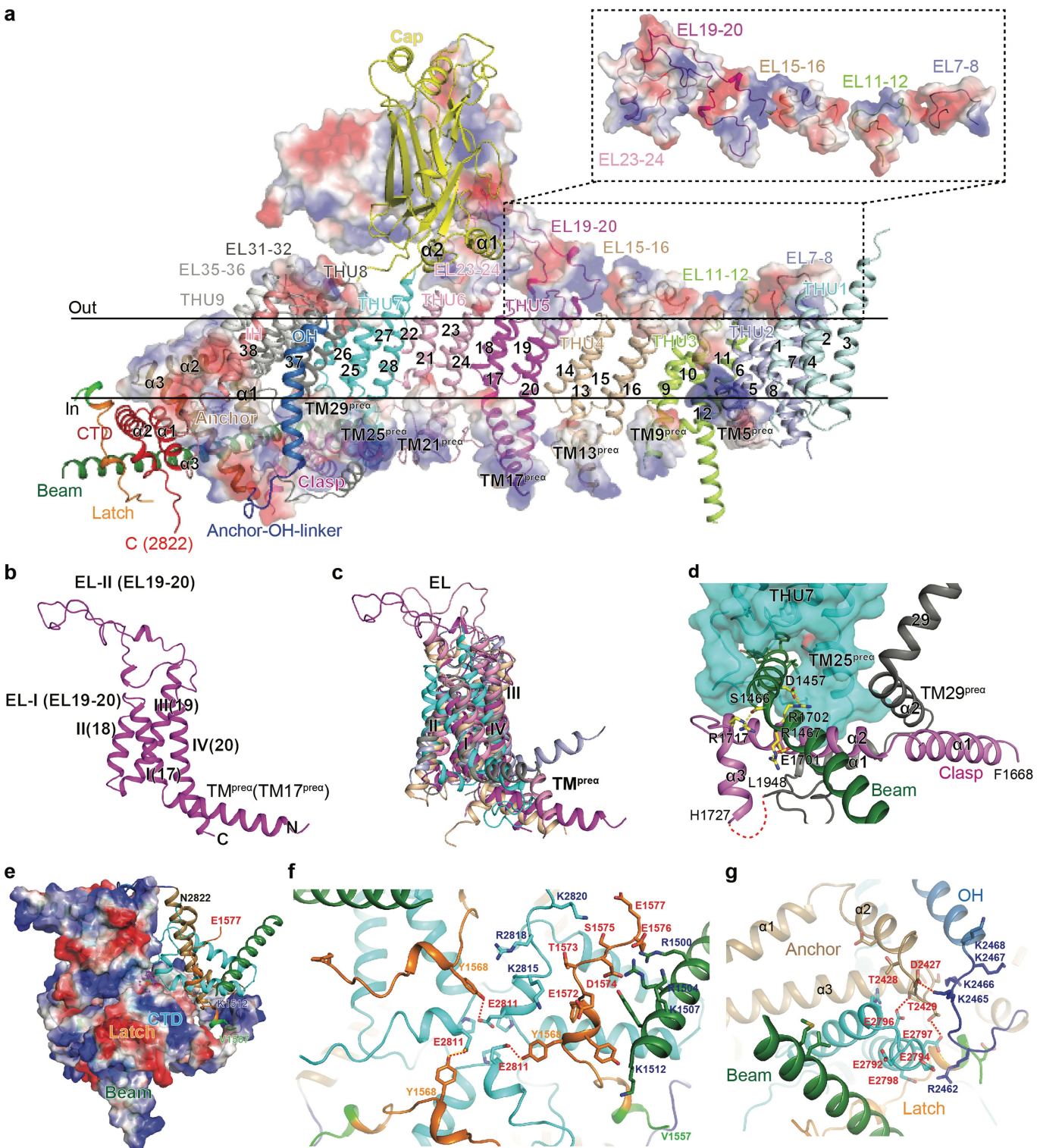


Extended Data Fig. 3 | Flowchart of electron-microscopy data processing. Details of data processing are described in the ‘Imaging processing’ section of the Methods.



Extended Data Fig. 4 | Local electron-microscopy density of the indicated domains of PIEZO2. The helices are shown in cartoon representation with side chains as sticks. The cryo-EM density is shown as grey mesh. Clearly resolved residues with bulky side chains—for example, phenylalanine, tryptophan, tyrosine, proline and histidine—are labelled.

The three pore-lining inner helices are shown in both side and top views to highlight the side-chain density of F2754, which forms a transmembrane gate, and E2757, which controls ion-permeation properties. The N-acetylglucosamine (NAG) groups that were modelled onto residues N769, N1030, N1037 and N2642 are labelled.



Extended Data Fig. 5 | See next page for caption.

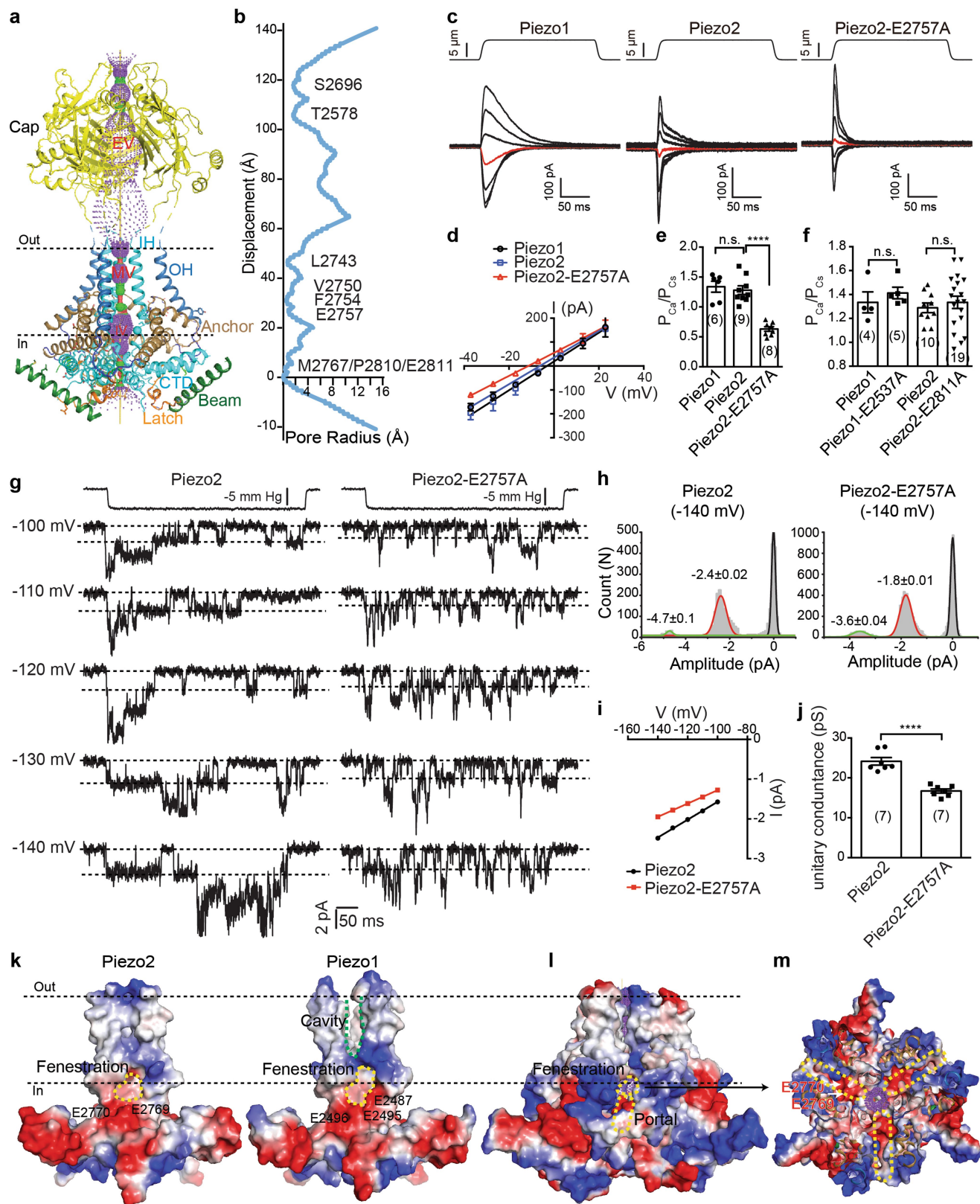
Extended Data Fig. 5 | The structure of PIEZO2 and the THU organization.

a, A protomer structure of PIEZO2 is presented in a format in which its transmembrane helices roughly adopt a planar configuration. The extracellular loops and intracellular membrane-parallel helices are shown in surface electrostatic potential. Notably, except THU1, which has a short N terminus of seven residues, each of the other eight THUs is preceded by a membrane-parallel helix, which connects perpendicularly to the first transmembrane helices. These intracellular membrane-parallel helices (including TM5^{pre- α} , TM9^{pre- α} , TM13^{pre- α} , TM17^{pre- α} , TM21^{pre- α} , TM25^{pre- α} , TM29^{pre- α} , clasp ^{α 1- α 2} and anchor ^{α 3}) collectively form an intracellular helical layer with the hydrophobic side facing the membrane side. The enlarged view of the EL7–8, EL11–12, EL15–16, EL19–20 and EL23–24 illustrates the flattened arrangement that is formed by these extracellular loops leaning against each other, except that EL19–20 sits on top of EL23–24. Such an organization might help to stabilize the blade and facilitate conformational propagation from the distal blade to the central region. **b**, THU5 is used as a typical example to show the organization pattern of the left-handed bundle of four transmembrane helices and the preceding membrane-parallel helix. **c**, Overlay of THU2 and THU4–THU7 (colour-coded as in **a**), showing the similar folding pattern. **d**, Intertwined interaction of the distal beam domain, THU7 and the clasp domain. The residues involved in forming polar interactions are shown in yellow. THU7 is shown in surface representation. The distal part of the beam is apparently kinked at the position of S1466 and buried within a space enclosed by the intracellular side of THU7 and the second and third α -helices of the clasp (clasp ^{α 2- α 3}). The clasp domain is composed of two long membrane-parallel helices (clasp ^{α 1- α 2}) to form an L-shaped helical structure, and a short helix (clasp ^{α 3}) that is positioned underneath the kink position of the beam. The beam and clasp domains are intertwined together with hydrogen-bond interactions between D1457 and R1702, S1466 and R1717, and R1467 and E1701 for stabilization. The 280 unresolved residues (1728–1947) that link the clasp ^{α 3} and TM29^{pre- α 1- α 2}

helices (indicated by the red dashed line) might provide additional interactions and regulation at the distal end of the beam.

e, Bottom view of the trimeric central region comprising the beam, the CTD and the latch domain. Two subunits are presented in surface electrostatic potential, and the other subunit is shown in ribbon representation. The proximal end of the beam directly contacts the hairpin-like CTD positioned on top, and connects to the perpendicularly crossed latch domain through 42 unresolved residues (1513–1556).

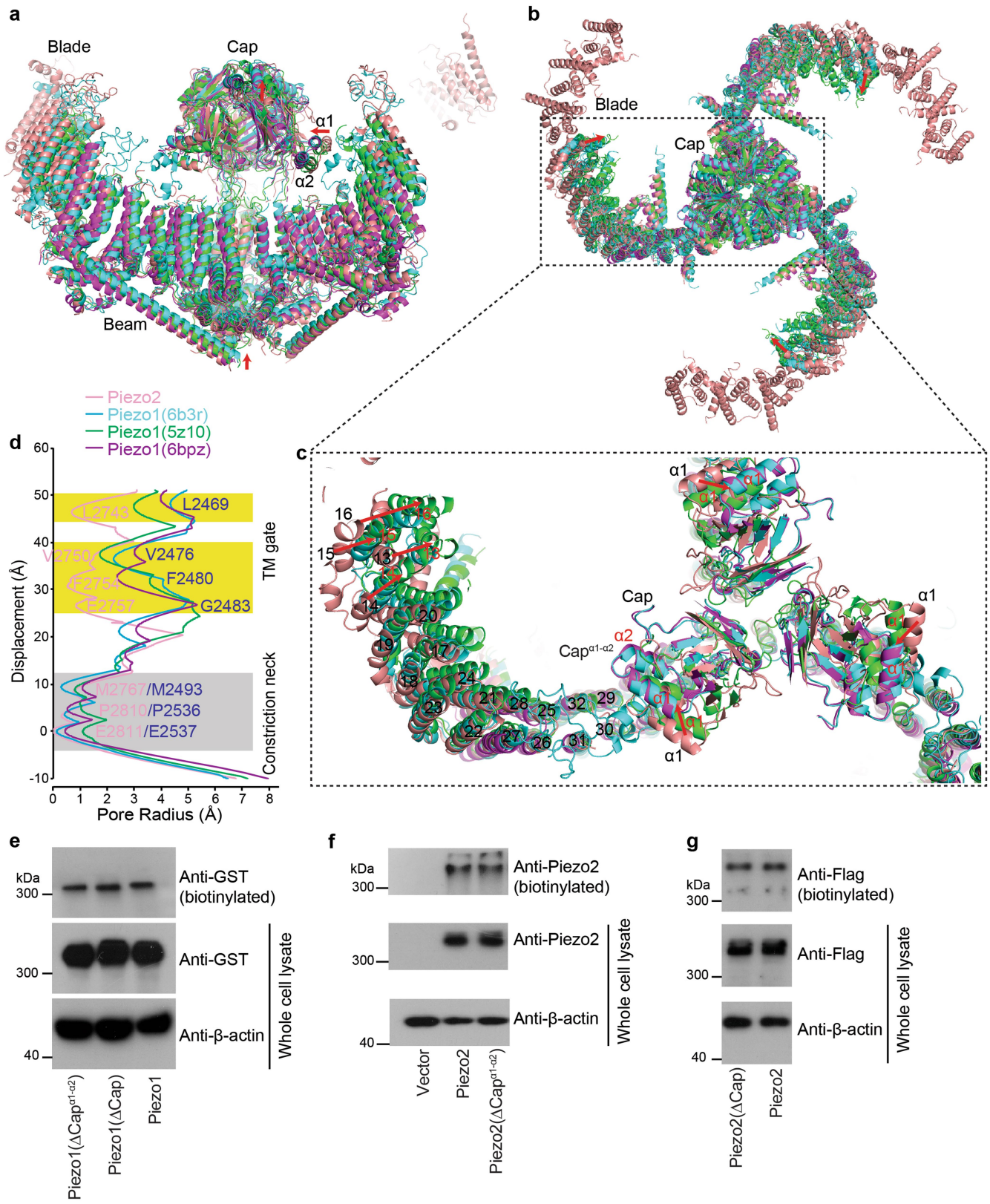
f, Ribbon diagram showing positively charged (blue) and negatively charged (red) residues that contribute to the negative surface potential of the latch domain and positive surface potential of the beam and CTD (as shown in **e**). The C-terminal section of the latch domain is rich in negatively charged and polar residues (1572–ETDSEE–1577) and is sandwiched in between the beam and the CTD with clusters of positively charged residues (R1500, R1504, K1507 and K1512 in the beam and K2815, R2818 and K2820 in the C-terminal tail). Y1568 in the latch domain points towards the putative intracellular exit of the central pore and forms hydrogen bonds with E2811, which contributes to the cytosolic constriction neck. **g**, Ribbon diagram showing the intertwined polar interactions of the indicated structural domains. The long membrane-parallel anchor ^{α 3} sits right on top of the CTD-hairpin plane and connects to the outer helix through a lysine-rich anchor-outer-helix linker (2456-KRYPQPRGQKKKK-2468), which forms interactions with the polar-residue-rich anchor ^{α 2- α 3} turn (2426-TDTT-2430), the glutamate-rich region of the CTD ^{α 1- α 2}-turn (2789-ETGELEEED-2798) and the N-terminal section of the latch domain. Several pairs of hydrogen bonds, including D2427–K2465, T2428–E2796 and T2429–E2797, might help to facilitate the intertwined interactions. The corresponding anchor-outer-helix linker in PIEZO1 is critical for mediating regulation by the sarco/endoplasmic reticulum Ca^{2+} -ATPase (SERCA), which binds to both PIEZO1 and PIEZO2.



Extended Data Fig. 6 | See next page for caption.

Extended Data Fig. 6 | The central ion-conducting pore and lateral portals of PIEZO2. **a**, Ribbon diagram showing the pore module (comprising the outer helix, cap, inner helix and CTD) together with the anchor, latch and beam domains. The central solvent-accessible pathway is marked with a dotted mesh (purple, green and red) generated by the program HOLE (pore radius: red, $<1\text{ \AA}$; green, $<2\text{ \AA}$; purple, $>2\text{ \AA}$). The extracellular vestibule (EV), membrane vestibule and intracellular vestibule are labelled. **b**, Pore radius along the central axis of the ion-conduction pathway of PIEZO2. The residues that form constriction sites are labelled. **c**, Representative traces of poking-evoked whole-cell currents in PIEZO1-KO-HEK cells transfected with the indicated constructs. Traces were recorded in an intracellular solution containing 149 mM caesium methanesulfonate and 1 mM CsCl, and an extracellular solution containing 50 mM calcium gluconate and 0.5 mM CaCl₂. Currents were elicited from -30 to $+30$ mV with a change of 10 mV at every step. The red trace represents the current elicited at 0 mV. The number of recorded cells is shown in **e**. **d**, Linear regression fit of average *I*–*V* relationships of whole-cell currents of the indicated constructs recorded under the conditions described in **c**. The liquid junction potential of 7.1 mV was subtracted. The number of recorded cells is shown in **e**. **e**, Scatter plots of $P_{\text{Ca}}/P_{\text{Cs}}$ of the indicated constructs. Data are mean \pm s.e.m. and the number of cells tested is labelled. One-way ANOVA: $P(\text{PIEZO1} \text{ versus } \text{PIEZO2}) = 0.8323$ (not significant; NS); $****P(\text{PIEZO2} \text{ versus } \text{PIEZO2(E2757A)}) < 0.0001$. **f**, Scatter plots of $P_{\text{Ca}}/P_{\text{Cs}}$ of the indicated constructs. Data are mean \pm s.e.m. and the

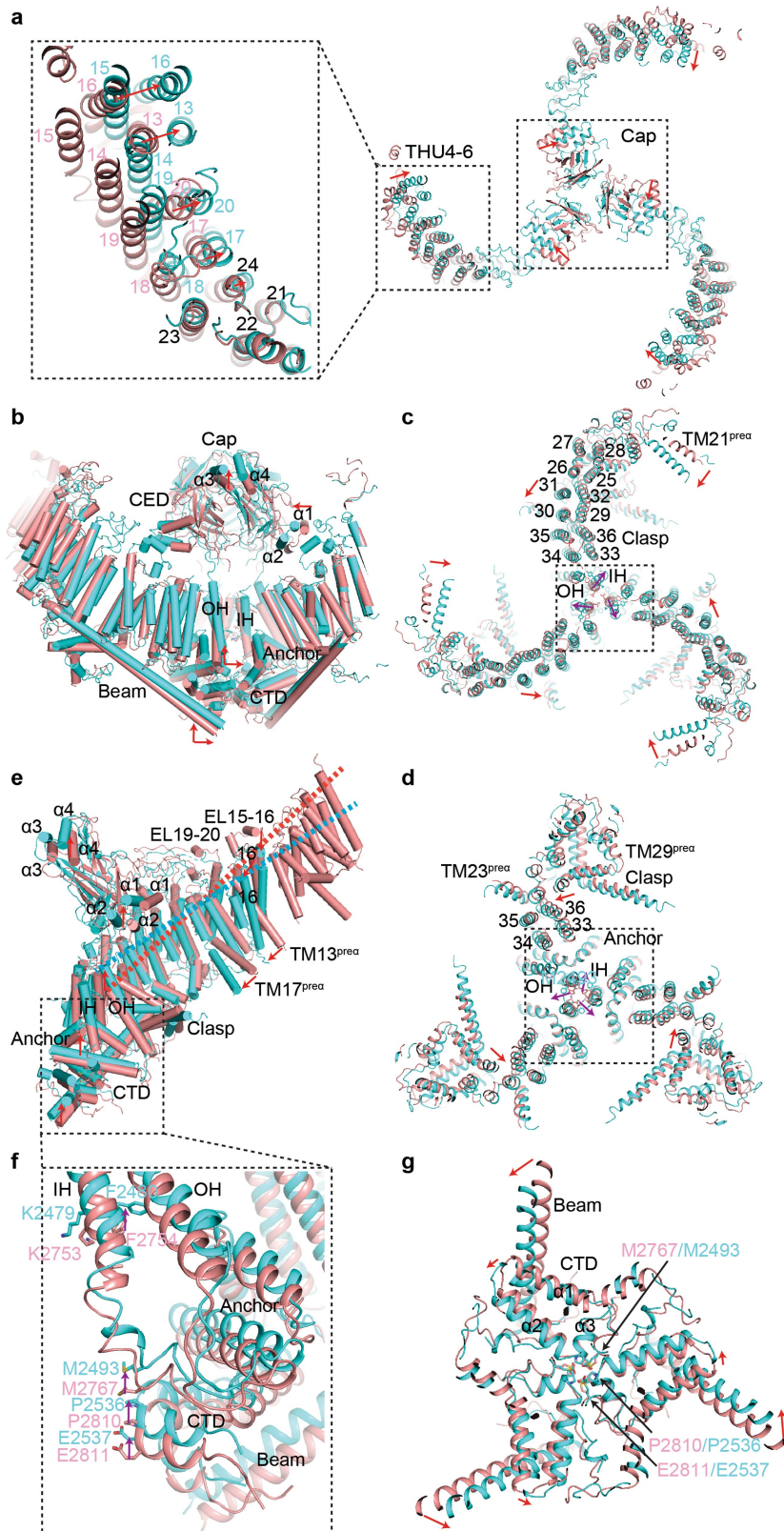
number of cells tested is labelled. Two-tailed unpaired Student's *t*-test: $P(\text{PIEZO1} \text{ versus } \text{PIEZO1(E2537A)}) = 0.4353$ (NS); $P(\text{PIEZO2} \text{ versus } \text{PIEZO2(E2811A)}) = 0.5566$ (NS). **g**, Representative stretch-evoked single-channel current traces recorded at the indicated holding voltages in PIEZO1-KO-HEK cells transfected with constructs expressing either PIEZO2 (seven cells recorded with currents) or PIEZO2(E2757A) (seven cells recorded with currents). **h**, Histogram analysis of the single-channel conductance from current traces recorded at -140 mV. **i**, Linear plots of the *I*–*V* relationships of the indicated constructs. **j**, Scatter plots of the slope of the single-channel conductance of the indicated constructs. Data are mean \pm s.e.m. and the number of cells tested is labelled. Two-tailed unpaired Student's *t*-test: $****P(\text{PIEZO2} \text{ versus } \text{PIEZO2-E2757A}) < 0.0001$. **k**, Surface electrostatic potential representation of the inner helix–CTD-enclosed central pore of PIEZO2 and PIEZO1, showing the hydrophobic transmembrane pore, intracellular fenestration site and the lateral negative surface potential that is contributed by the indicated negatively charged residues (which determine the properties of the pore). Notably, PIEZO1 has apparent membrane-facing cavities (indicated by the green dashed line) between two inner helices. **l**, **m**, Surface electrostatic potential representations of the inner helix–CTD-enclosed central pore together with the surrounding anchor, beam and latch domains, showing the intracellular fenestration sites and lateral portals in either a side-view (**l**) or top-view (**m**) section at the position indicated by the arrow in panel **l**. The fenestrations and lateral portals are outlined with yellow dashed lines.



Extended Data Fig. 7 | See next page for caption.

Extended Data Fig. 7 | Structural comparison between PIEZO1 and PIEZO2. **a, b**, Side (a) or top (b) overlay view of PIEZO2 (salmon), PIEZO1 (PDB: 6B3R) (cyan), PIEZO1 (PDB: 5Z10) (green) and PIEZO1 (PDB: 6BPZ) (purple). **c**, An enlarged view of the cap and blade regions zoomed in at the $\text{cap}^{\alpha 1-\alpha 2}$ position. Red arrows indicate the shifted positions of PIEZO1 relative to PIEZO2. The clockwise twist and upward displacement of the cap domain is more robust in PIEZO1 (PDB: 6B3R) and PIEZO1 (PDB: 6BZ) than in PIEZO1 (PDB: 5Z10), whereas the lateral displacement of the distal blade of TM13–TM24 is relatively stronger in PIEZO1 (PDB: 5Z10) than in PIEZO1 (PDB: 6B3R). TM13–TM24 of PIEZO1 (PDB: 6BPZ) were not modelled. **d**, Pore radius along the inner helix–CTD central axis of the ion-permeation pore of the indicated PIEZO2 and PIEZO1 structures. The residues that form constriction sites are labelled. Notably, the transmembrane gates of all three PIEZO1 structures determined in different detergents including GDN (PDB: 6B3R), digitonin (PDB: 6BPZ) and C₁₂E₁₀ (PDB: 5Z10) have dilated transmembrane gates relative to that of PIEZO2 determined in GDN. Furthermore, dilation of the transmembrane gate of PIEZO1 is closely

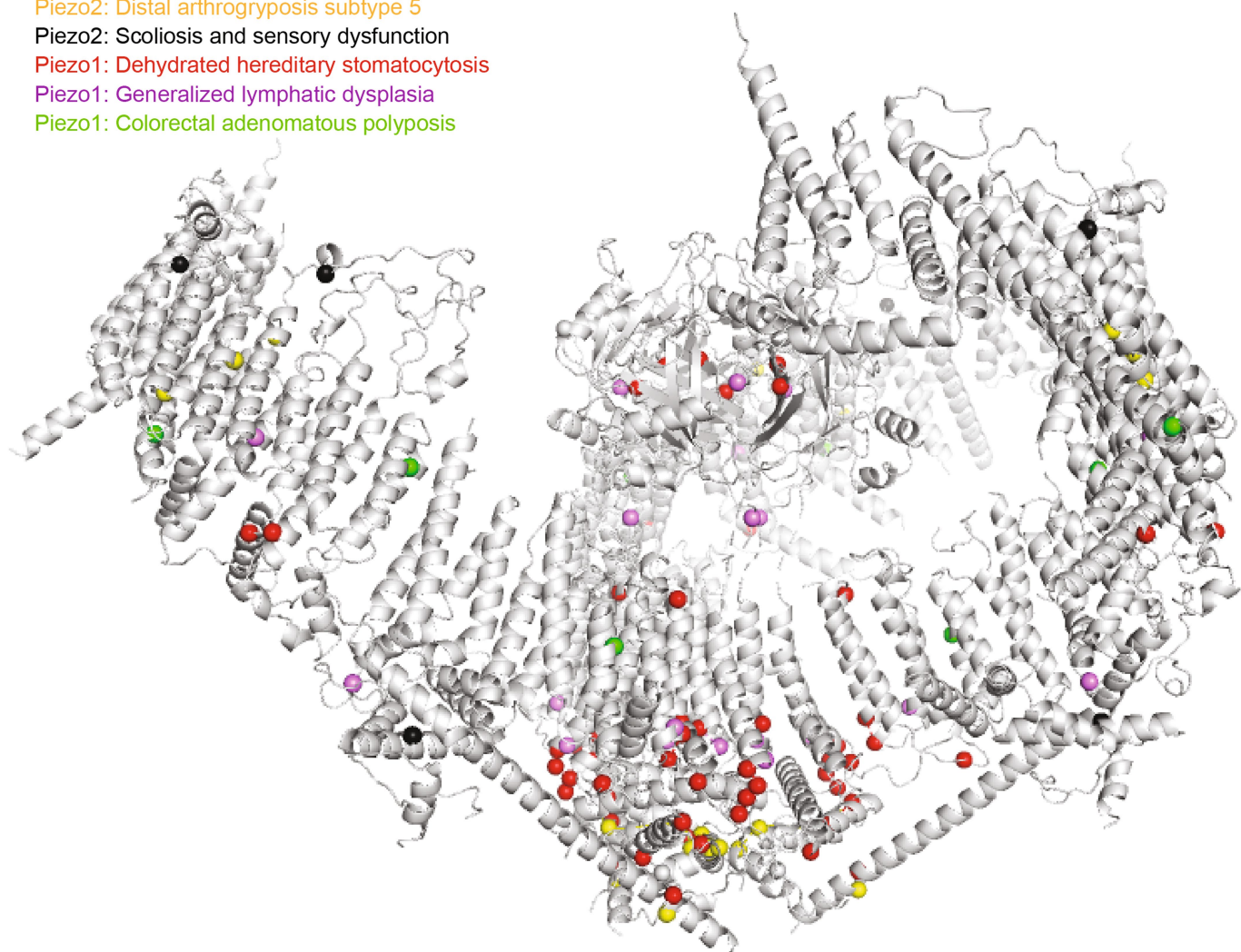
correlated with the displacement of the cap among the three PIEZO1 structures (**a–d**). For example, compared to PIEZO1 (PDB: 5Z10), PIEZO1 (PDB: 6B3R) and PIEZO1 (PDB: 6BPZ) show relatively stronger displacement of the cap domain (for example, the $\text{cap}^{\alpha 1-\alpha 2}$ region) (**c**) and concurrent larger expansion of the upper transmembrane gate of L2469 (**d**). Given that PIEZO2 is much less responsive to stretch stimulation, we speculate that surface tension generated during cryo-EM sample preparation might lead to opening of the transmembrane pore of PIEZO1, but not PIEZO2. **e–g**, Western blotting of the biotinylated or whole-cell lysate samples derived from HEK293T cells transfected with the indicated constructs using the indicated antibodies. The PIEZO2 antibody in **f** was raised against the peptide corresponding to residues 2662–2674 in the cap domain of mouse PIEZO2, and could not recognize the PIEZO2(Δ cap) protein (data not shown). Thus, the anti-Flag antibody was used to detect the PIEZO2-mRuby2-Flag and PIEZO2(Δ cap)-mRuby2-Flag proteins in **g**. The anti- β -actin antibody detected β -actin for a loading control. The experiment was independently repeated twice or three times with similar results.



Extended Data Fig. 8 | Structural comparison between PIEZO1 (PDB: 6B3R) and PIEZO2. **a, c, d, g,** Top views of the superimposed PIEZO2 (salmon) and PIEZO1 (PDB: 6B3R) (cyan) structures zoomed in at either cap $\alpha^1-\alpha^2$ (**a**), the PIEZO2(L2743) residue (**c**), the PIEZO2 (F2754) residue (**d**) or the cytosolic constriction site of PIEZO2(M2767/P2810/E2811) (**g**). The boxed regions at the centre of **a, c** and **d** are presented in enlarged views in Fig. 4a–c, respectively. Arrows indicate the displacement direction of PIEZO1 relative to PIEZO2; red arrows show the displacement of the cap or the blade domains, whereas purple arrows show the displacement

of the side chain of the indicated residues. For example, TM16 of PIEZO1 has a lateral displacement of about 12 Å relative to that of PIEZO2 (**a**). **b, e,** Side views of the superimposed PIEZO2 (salmon) and PIEZO1 (PDB: 6B3R) (cyan) trimers (**b**) or monomers (**e**). Red arrows indicate the displacement direction of PIEZO1 relative to PIEZO2. The blue and red dashed lines in **e** indicate the flatness of the curved transmembrane region of the blade. **f,** The upward displacement associated with the beam, CTD, anchor and outer helix might contribute to the upward displacement of the cytosolic constriction neck, the transmembrane gate and the inner helix.

Piezo2: Distal arthrogryposis subtype 5
Piezo2: Scoliosis and sensory dysfunction
Piezo1: Dehydrated hereditary stomatocytosis
Piezo1: Generalized lymphatic dysplasia
Piezo1: Colorectal adenomatous polyposis



Extended Data Fig. 9 | Mapping disease-causing mutations in human PIEZO1 and PIEZO2 onto the mouse PIEZO2 structure. The dots in different colours represent the disease-causing residues labelled in the protein sequence shown in Supplementary Fig. 2.

Extended Data Table 1 | Cryo-EM data collection, refinement and validation statistics

Piezo2 (EMDB-9975) (PDB 6KG7)	
Data collection and processing	
Magnification	81000
Voltage (kV)	300
Electron exposure (e-/Å ²)	50
Defocus range (μm)	-1.5 ~ -2.5
Pixel size (Å)	1.401
Symmetry imposed	C3
Initial particle images (no.)	2,721,959
Final particle images (no.)	131,550 / 108,781 / 386,144 / 347,108*
Map resolution (Å)	3.80 / 3.86 / 3.64 / 3.77*
FSC threshold	0.143
Map resolution range (Å)	5.5-3.0 / 5.5-3.0 / 5.5-3.0 / 5.5-3.0*
Refinement	
Initial model used (PDB code)	5Z10 / 6B3R / 4RAX
Model resolution (Å)	3.7
FSC threshold	0.5
Map sharpening <i>B</i> factor (Å ²)	-146 / -147 / -140 / -167*
Model composition	
Non-hydrogen atoms	44892
Protein residues	5451
Ligands	12
<i>B</i> factors (Å ²)	
Protein	122.15
Ligand	171.28
R.m.s. deviations	
Bond lengths (Å)	0.003
Bond angles (°)	0.583
Validation	
MolProbity score	1.88
Clashscore	9.16
Poor rotamers (%)	0.00
Ramachandran plot	
Favored (%)	94.27
Allowed (%)	5.73
Disallowed (%)	0.00

*indicates the value for the overall map and the focused maps of central region, blade and distal blade, respectively.

Corresponding author(s): 2019-03-04606A

Last updated by author(s): Jul 12, 2019

Reporting Summary

Nature Research wishes to improve the reproducibility of the work that we publish. This form provides structure for consistency and transparency in reporting. For further information on Nature Research policies, see [Authors & Referees](#) and the [Editorial Policy Checklist](#).

Statistics

For all statistical analyses, confirm that the following items are present in the figure legend, table legend, main text, or Methods section.

n/a Confirmed

- The exact sample size (n) for each experimental group/condition, given as a discrete number and unit of measurement
- A statement on whether measurements were taken from distinct samples or whether the same sample was measured repeatedly
- The statistical test(s) used AND whether they are one- or two-sided
Only common tests should be described solely by name; describe more complex techniques in the Methods section.
- A description of all covariates tested
- A description of any assumptions or corrections, such as tests of normality and adjustment for multiple comparisons
- A full description of the statistical parameters including central tendency (e.g. means) or other basic estimates (e.g. regression coefficient) AND variation (e.g. standard deviation) or associated estimates of uncertainty (e.g. confidence intervals)
- For null hypothesis testing, the test statistic (e.g. F , t , r) with confidence intervals, effect sizes, degrees of freedom and P value noted
Give P values as exact values whenever suitable.
- For Bayesian analysis, information on the choice of priors and Markov chain Monte Carlo settings
- For hierarchical and complex designs, identification of the appropriate level for tests and full reporting of outcomes
- Estimates of effect sizes (e.g. Cohen's d , Pearson's r), indicating how they were calculated

Our web collection on [statistics for biologists](#) contains articles on many of the points above.

Software and code

Policy information about [availability of computer code](#)

Data collection

AutoEMation II

Data analysis

MotionCor2, CTFFIND3, RELION-3.0, Gctf, Resmap, PHENIX, Coot, HOLE, Chimera, Pymol, GraphPad Prism 6

For manuscripts utilizing custom algorithms or software that are central to the research but not yet described in published literature, software must be made available to editors/reviewers. We strongly encourage code deposition in a community repository (e.g. GitHub). See the Nature Research [guidelines for submitting code & software](#) for further information.

Data

Policy information about [availability of data](#)

All manuscripts must include a [data availability statement](#). This statement should provide the following information, where applicable:

- Accession codes, unique identifiers, or web links for publicly available datasets
- A list of figures that have associated raw data
- A description of any restrictions on data availability

Provide your data availability statement here.

Field-specific reporting

Please select the one below that is the best fit for your research. If you are not sure, read the appropriate sections before making your selection.

Life sciences Behavioural & social sciences Ecological, evolutionary & environmental sciences

For a reference copy of the document with all sections, see nature.com/documents/nr-reporting-summary-flat.pdf

Life sciences study design

All studies must disclose on these points even when the disclosure is negative.

Sample size	For all functional experiments, the sample sizes represent the number of cells used for experiments and data analysis. And the sample size is determined based on the consistency of the recordings
Data exclusions	No data was excluded in patch clamp recordings.
Replication	All experimental findings were reliably reproduced.
Randomization	For structure refinement and model validation, all particles were randomly split into two groups, one for refinement and the other for validation. For functional experiments, cells with fluorescence were randomly selected for recording or imaging.
Blinding	The investigators were blinded to group allocation during data collection and analysis

Reporting for specific materials, systems and methods

We require information from authors about some types of materials, experimental systems and methods used in many studies. Here, indicate whether each material, system or method listed is relevant to your study. If you are not sure if a list item applies to your research, read the appropriate section before selecting a response.

Materials & experimental systems

n/a	Involved in the study
<input type="checkbox"/>	<input checked="" type="checkbox"/> Antibodies
<input type="checkbox"/>	<input checked="" type="checkbox"/> Eukaryotic cell lines
<input checked="" type="checkbox"/>	<input type="checkbox"/> Palaeontology
<input checked="" type="checkbox"/>	<input type="checkbox"/> Animals and other organisms
<input checked="" type="checkbox"/>	<input type="checkbox"/> Human research participants
<input checked="" type="checkbox"/>	<input type="checkbox"/> Clinical data

Methods

n/a	Involved in the study
<input type="checkbox"/>	<input checked="" type="checkbox"/> ChIP-seq
<input checked="" type="checkbox"/>	<input type="checkbox"/> Flow cytometry
<input checked="" type="checkbox"/>	<input type="checkbox"/> MRI-based neuroimaging

Antibodies

Antibodies used

rabbit anti-GST (Millipore, 1:3,000, Cat#: 2622S), rabbit anti-β-actin (Cell Signaling Technology, 1:3,000, Cat#: 4970S), peroxidase-conjugated anti-rabbit IgG secondary antibody (CST, 1:10,000,Cat#: 7074S)

Validation

Describe the validation of each primary antibody for the species and application, noting any validation statements on the manufacturer's website, relevant citations, antibody profiles in online databases, or data provided in the manuscript.

Eukaryotic cell lines

Policy information about [cell lines](#)

Cell line source(s)

HEK293T, P1-KO-HEK293 cell line

Authentication

HEK293T was from ATCC, P1-KO-HEK293 cell line was from Ardem Patapoutian lab, which was validated as mentioned in Lukacs 2015(PMID:2638713).

Mycoplasma contamination

Test negative.

Commonly misidentified lines (See [ICLAC](#) register)

No commonly misidentified cell lines were used.